SCORE-BASED FREE-FORM ARCHITECTURES FOR HIGH-DIMENSIONAL FOKKER-PLANCK EQUATIONS

Anonymous authors
Paper under double-blind review

ABSTRACT

Deep learning methods, which incorporate the PDE residual as loss function, have recently emerged to solve Fokker-Planck equations. Without reference solutions, proper normalization condition is required to avoid a trivial solution. However, soft constraints require careful balancing of multi-objective loss function, and specific network architectures may limit representation capacity. In this paper, we propose a novel framework: *Fokker-Planck neural network (FPNN)* that adopts a score PDE loss to decouple the score learning and the density normalization into two stages. Our method is mesh-free and causality-free, allowing for free-form network architectures to model the unnormalized density and strictly satisfy normalization constraints by post-processing. We demonstrate the effectiveness on various high-dimensional steady-state Fokker-Planck (SFP) equations, achieving superior accuracy and over a 20× speedup compared to state-of-the-art methods. Without any labeled data, FPNNs achieve the mean absolute percentage error (MAPE) of 11.36%, 13.87% and 12.72% for 4D Ring, 6D Unimodal and 6D Multi-modal problems respectively, requiring only 256, 980, and 980 parameters. Experimental results highlights the potential as a universal fast solver for handling more than 20-dimensional SFP equations, with great gains in efficiency, accuracy, memory and computational resource usage.

1 INTRODUCTION

The Fokker–Planck (FP) equation governs the time-varying response probability density function (PDF) of dynamical systems driven by stochastic processes (Risken & Caugheyz, 1991). It finds wide applications in statistical physics, chemistry, biology, mathematical finance, and structural dynamics (De Decker & Nicolis, 2020; Tu et al., 2020; Hu et al., 2021; Boghosian et al., 2017). Solving FP equations presents three main challenges: high-dimensional variables, unbounded spatial domains, and the normalization condition (NC). Traditional grid-based methods are constrained by the curse of dimensionality, while path integral methods and Monte Carlo (MC) simulations are significantly limited by noise and computational complexity (Naess & Moe, 2000; Elman et al., 2014; Chen & Majda, 2017; Natarajan et al., 2021).

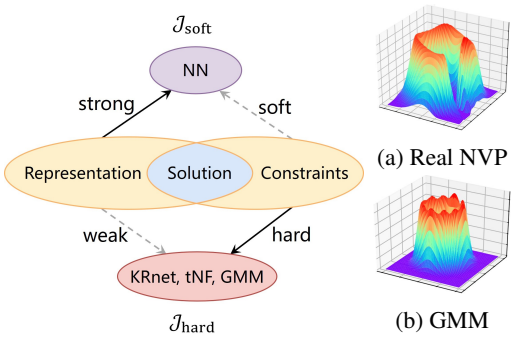

Figure 1: *Left*: Strengths and weaknesses for existing models. *Right*: Real NVP and GMM with 16 components fail to learn the ring function. The former consistently leaves a gap, while the latter exhibits numerous irregular protrusions.

Deep learning methods, with their grid-free, causality-free, and feature-learning capabilities, have demonstrated potential in addressing high-dimensional partial differential equations (PDEs) (Han et al., 2018; Yu et al., 2018; Sirignano & Spiliopoulos, 2018; Liu et al., 2024). Among these promising methods, physics-informed neural networks (PINNs) (Raissi et al., 2019) leverage automatic differentiation to enforce the physical constraints of underlying PDEs and achieve great success in various problems, such as the Navier-Stokes equation, Burgers' equation, Schrödinger equation, etc.

However, for steady-state Fokker-Planck (SFP) equations, PINN faces a new challenge: the zero solution also satisfies this equation and directly minimizing the plain PDE loss will quickly collapse the model to a trivial solution.

To mitigate this issue, data-driven methods guide the neural network (NN) to the desired solution by introducing labeled data or Kullback-Leibler divergence terms (Zhai et al., 2022; Chen et al., 2021). For 4D Ring problem, FP solver (Zhai et al., 2022) utilizes the direct Monte Carlo method with a very large number of particles (10^{10} sample points) to obtain 10^4 reference points. This method is computationally intensive and errors in the reference solutions may inversely limit the model's performance.

Table 1: Deep learning methods for SFP equations.

Methods	**Loss function**	**Model**	**Arbitrary NN?**	**Whether strictly satisfy NC?**
Data-Driven	$\mathcal{J}_{\text{plain}} + \lambda \mathcal{J}_{\text{label}}$	$p_\theta(\boldsymbol{x}) = p_{\text{NN}}(\boldsymbol{x};\theta)$	✓	✗
Normalization Condition	$\mathcal{J}_{\text{plain}} + \lambda \mathcal{J}_{\text{norm}}$	$p_\theta(\boldsymbol{x}) = p_{\text{NN}}(\boldsymbol{x};\theta)$	✓	✗
	$\mathcal{J}_{\text{plain}}(p_\theta)$	$p_\theta(\boldsymbol{x}) = p_{\text{KRnet}}(\boldsymbol{x};\theta),\ p_{\text{GMM}}(\boldsymbol{x};\theta),\ p_{\text{TNN}}(\boldsymbol{x};\theta)\cdots$	✗	✓
	$\mathcal{J}_{\text{score}}(\widetilde{p}_\theta)$	$\widetilde{p}_\theta(\boldsymbol{x}) = \widetilde{p}_{\text{NN}}(\boldsymbol{x};\theta),\ p_\theta(\boldsymbol{x}) = \frac{\widetilde{p}_\theta(\boldsymbol{x})}{\int \widetilde{p}_\theta(\boldsymbol{y})d\boldsymbol{y}}$	✓	✓

Another strategy that does not require labeled data is to impose normalization constraints in soft or hard manner. Soft constraints prevent zero solutions by adding a normalization penalty term that enforces the density integral to unity (Alhussein et al., 2023). While the normalization condition prevents the approximate solution from being zero across the entire domain, minimizing the plain PDE loss still has a tendency toward the trivial solution. These conflicting forces result in tortuous optimization dynamics (Wang et al., 2024; Al-Aradi et al., 2022), requiring delicate balancing of the multi-objective loss function. Specialized structures, such as normalizing flows (Dinh et al., 2016; Tang et al., 2022; Feng et al., 2022) and Gaussian mixture model (GMM) (Anderson & Farazmand, 2024), are developed to represent density functions and enforce hard constraints. These methods shrink the trial solution space and compromise the representation capability, leading to significant errors and computational burden when learning certain PDFs.

In summary, the former method requires manual balancing of multi-objective losses, while the latter may constrain the model's representation capacity. As shown in Figure 1, the ideal method strictly satisfies normalization constraints without sacrificing representation capacity. To the best of our knowledge, there is no effective approach to handle this conflict. In this paper, we propose a novel framework: Fokker-Planck Neural Network (FPNN) to decouple the fitting and normalizing stages through score PDE loss. FPNN efficiently solves high-dimensional SFP equations and offers the following advantages:

Adaptive Domain for Complex Systems. High-dimensional state spaces often exhibit intricate dynamics and interaction patterns. To accurately identify critical features and high-probability regions, we use the stochastic Runge–Kutta (SRK) method with strong order 1.5 to generate steady-state training data and adaptively determine the appropriate domain for SFP problems.

Flexible Scaling for Small Solutions. Since the probability density is non-negative and must integrate to unity over the spatial domain, the solution to high-dimensional problems is typically quite small and networks struggle to resolve such small yet meaningful scales directly. FPNN employs a score PDE loss, allowing the network to freely choose an appropriate scale and learn the unnormalized density. This effect of "data standardization" is infeasible for existing methods without labeled data or prior knowledge.

Efficient Enforcement of Normalization Constraints. The score loss allows free-form network architectures to strictly satisfy normalization constraints. FPNN avoids evaluating the density function integral during training process and instead calculates the normalizing constant by post-processing.

Scalability and Improvements in Optimization Dynamics. Without any labeled data or the enforcement of zero boundary conditions, we successfully solve various 4-20 dimensional SFP equations for complex physical systems. FPNN circumvents the normalization condition in loss function which causes difficulty in training, and substantially improves optimization dynamics.

Therefore, a large learning rate ($l = 0.01$) is allowed for fast descent and stable convergence, and FPNN achieves over 20× speedup compared to state-of-the-art methods. We get the MAPE of 11.36%, 13.87% and 12.72% for 4D Ring, 6D Unimodal and 6D Multi-modal problems respectively, requiring only 256, 980, and 980 parameters. Our framework demonstrates substantial gains in efficiency, accuracy, and memory usage.

2 PRELIMINARIES

Fokker–Planck equation. Consider stochastic differential equations (SDEs) (Oksendal, 2013) of the form

$$d\mathbf{X} = \boldsymbol{\mu}(\mathbf{X})dt + \boldsymbol{\sigma}(\mathbf{X})d\mathbf{W}_t, \tag{1}$$

where the drift coefficient $\boldsymbol{\mu}(\mathbf{X}) \in \mathbb{R}^d$ is a vector field, $\boldsymbol{\sigma}(\mathbf{X}) \in \mathbb{R}^{d\times M}$ is a matrix-valued function and $\mathbf{W}_t$ is an M-dimensional standard Wiener process. The density function $p(\boldsymbol{x})$[1] of state variable $\mathbf{X}$ represents an invariant distribution, satisfying the steady-state Fokker-Planck (SFP) equation:

$$\begin{gathered}\frac{\partial p(\boldsymbol{x})}{\partial t} = \mathcal{L}p := -\sum_{i=1}^{d}\frac{\partial(p\mu_i)}{\partial x_i} + \sum_{i=1}^{d}\sum_{j=1}^{d}\frac{\partial^2(D_{i,j}p)}{\partial x_i \partial x_j} = -\nabla\cdot(p\boldsymbol{\mu}) + \nabla\cdot[\nabla\cdot(\boldsymbol{D}p)], \\ i.e. \quad \mathcal{L}p(\boldsymbol{x}) = 0, \qquad p(\boldsymbol{x}) \to 0 \quad (||\boldsymbol{x}|| \to \infty), \qquad \int_{\mathbb{R}^d} p(\boldsymbol{x})d\boldsymbol{x} = 1,\end{gathered} \tag{2}$$

where $\boldsymbol{x} \in \mathbb{R}^d$ is the spatial variable, $\boldsymbol{D}(\boldsymbol{x}) = \frac{1}{2}\boldsymbol{\sigma}(\boldsymbol{x})\boldsymbol{\sigma}(\boldsymbol{x})^T$ is the diffusion matrix, $\mathcal{L}$ denotes the Fokker-Planck differential operator and $||\boldsymbol{x}||$ indicates the ℓ_2 norm of $\boldsymbol{x}$.

Physics-informed neural networks. PINN is a deep neural network $p_\theta(\boldsymbol{x})$ to approximate the solution $p(\boldsymbol{x})$ with the universal approximation theorem (Hornik et al., 1989). The SFP equation in Eq. (2) can be expressed as,

$$\mathcal{L}p(\boldsymbol{x}) = 0 \quad \boldsymbol{x} \in \Omega, \qquad \mathcal{B}_i p(\boldsymbol{x}_i) = 0 \quad \boldsymbol{x}_i \in \partial\Omega_i, \qquad \mathcal{I}p = 1. \tag{3}$$

Here, $\mathcal{B}_i$ are boundary conditions (BCs) for boundaries $\partial\Omega_i \subset \Omega$, and the integral operator $\mathcal{I}$ represents the NC. These physical constraints are incorporated as regularization (typically mean-squared error terms) in the loss function. To accelerate model training and reduce violations of physical laws, hard constraints can be used to omit part loss terms.

Score-based generative model. Score matching (Hyvärinen & Dayan, 2005) is a popular method for learning unnormalized statistical models and score-based generative models have shown promising performance in both sample quality and sample efficiency, which can be combined with numerical SDE solvers or fast ODE solvers to generate samples (Song et al., 2021; Song & Ermon, 2020; Lu et al., 2022). Score loss are usually optimized by minimizing the Fisher divergence between the gradients of log-density functions (i.e., scores) and the ground truth scores from data, without handling the intractable partition functions (Song et al., 2020; Luo, 2022). This idea serves as the primary inspiration for our score PDE loss.

3 FOKKER–PLANCK NEURAL NETWORKS

Considering that optimization, data, and model form the cores of deep learning approaches, we introduce the FPNN framework through these three components. First, we define the score-based Fokker–Planck loss as the objective function to solve SFP equations. Then, steady-state data from true distribution is required to evaluate the score loss, for which we simulate SDEs using the SRK method. Finally, we briefly review the tensor neural network (TNN) and the multi-layer perceptron (MLP), implementing appropriate modifications to suit our task.

[1] We mainly focus on the SFP equation, where the stochastic system reaches an invariant equilibrium distribution and parameters $\boldsymbol{\mu}$, $\boldsymbol{\sigma}$ are independent of time t. Examples of PDEs, experimental settings, as well as expressions for $\boldsymbol{\mu}(\boldsymbol{x})$ and $\boldsymbol{\sigma}(\boldsymbol{x})$ can be found in Appendix C.

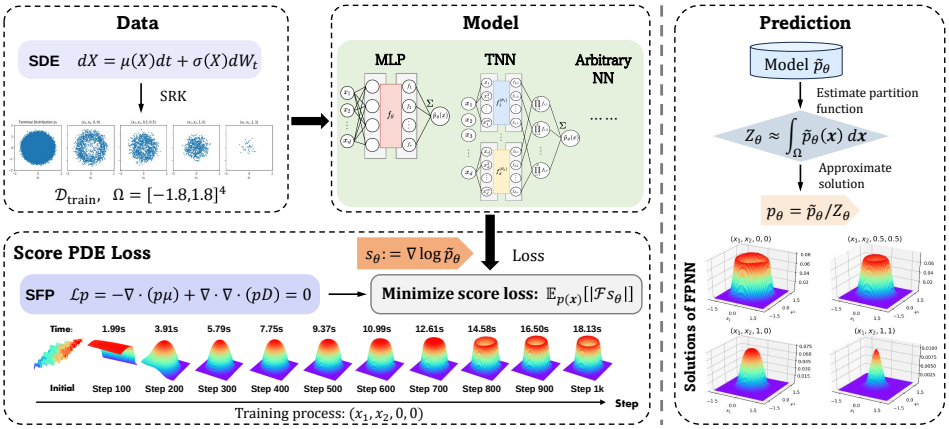

Figure 2: FPNN framework for high-dimensional SFP equations. We use the SRK method to simulate SDE for generating training dataset $\mathcal{D}_{\text{train}}$ and domain Ω. Then, the data is fed into a free-form architecture to produce the score. Next, we train the model by minimizing the score-based FP loss. With the trained model $\widetilde{p}_\theta$, we compute the partition function and perform normalization once to obtain the solution of SFP equation.

3.1 Score-based PDE loss

Score matching is originally designed for estimating unnormalized probability densities in machine learning, statistics, and signal processing. The score of density $p(\boldsymbol{x})$ is defined as $\nabla \log p(\boldsymbol{x})$. When the model learns a density $\widetilde{p}_\theta(\boldsymbol{x})$ with the partition function Z_θ, the approximate solution of SFP equation is a normalized density denoted by,

$$p_\theta(\boldsymbol{x}) = \frac{\widetilde{p}_\theta(\boldsymbol{x})}{Z_\theta}, \qquad Z_\theta = \int \widetilde{p}_\theta(\boldsymbol{x}) d\boldsymbol{x} \tag{4}$$

Note that since $\log p_\theta(\boldsymbol{x}) = \log \widetilde{p}_\theta(\boldsymbol{x}) - \log Z_\theta$ and $\nabla \log p_\theta(\boldsymbol{x}) = \nabla \log \widetilde{p}_\theta(\boldsymbol{x})$, we immediately conclude that $p_\theta(\boldsymbol{x})$ and $\widetilde{p}_\theta(\boldsymbol{x})$ share the same score, which does not depend on the intractable partition function Z_θ.

Inspired by this fact, we directly model the unnormalized density $\widetilde{p}_\theta$ and the score function $\boldsymbol{s}_\theta = \nabla \log \widetilde{p}_\theta$ using a neural network, and employ $\boldsymbol{s}_\theta$ to approximate the true score. Once we reformulate the plain PDE loss of SFP equations into a score-based form, our model can learn the correct score function and focus on the shape of PDF without handling NC. With the trained model $\widetilde{p}_\theta(\boldsymbol{x})$, we compute the partition function only once by post-processing and obtain the approximate solution $p_\theta(\boldsymbol{x})$ via Eq. (4).

Theorem 1 (Score-based FP loss)**.** *Assume the approximate solution $p_\theta(\boldsymbol{x})$ is differentiable and positive, satisfying regularity conditions*[2]*: for a fixed set of $(\boldsymbol{\mu}(\boldsymbol{x}), \boldsymbol{D}(\boldsymbol{x}))$, $\mathbb{E}[|\mathcal{L}p_\theta(\boldsymbol{x})|]$ is finite for any θ. Denote the model score function as $\boldsymbol{s}_\theta(\boldsymbol{x}) := \nabla \log \widetilde{p}_\theta(\boldsymbol{x})$ to approximate $\nabla \log p(\boldsymbol{x})$ and $p(\boldsymbol{x})$ is the true solution of SFP equation. The plain PDE loss can be expressed as the following up to a constant factor*

$$\mathbb{E}_{p(\boldsymbol{x})}[|\mathcal{F}\boldsymbol{s}_\theta(\boldsymbol{x})|] := \mathbb{E}_{\boldsymbol{x}\sim p(\boldsymbol{x})}[|\boldsymbol{s}_\theta(\boldsymbol{x}) \cdot \widetilde{\boldsymbol{\mu}}(\boldsymbol{x}) + \nabla \cdot \widetilde{\boldsymbol{\mu}}(\boldsymbol{x})|] \tag{5}$$

where $\widetilde{\boldsymbol{\mu}}(\boldsymbol{x}) := \boldsymbol{\mu}(\boldsymbol{x}) - \nabla \cdot \boldsymbol{D}(\boldsymbol{x}) - \boldsymbol{D}(\boldsymbol{x})\boldsymbol{s}_\theta(\boldsymbol{x})$ does not explicitly involve the density. $\mathcal{F}$ is named as the score-based FP operator, and the proposed PDE loss solely depends on the score $\boldsymbol{s}_\theta(\boldsymbol{x})$.

Proof in Appendix A and we further clarify the connection between the score PDE loss and score matching. By modeling the unnormalized density, we avoid the computational burden caused by frequently estimating Z_θ at each iteration, and also eliminate the interference of NC during training process. In this way, FPNN decouples the fitting and normalizing stages, ensuring continuous and efficient training process.

[2]Since solving FP equations with PINN is a well-posed problem, this result can be directly inferred from the loss function setup. Additionally, the loss functions $\mathbb{E}[|\mathcal{L}p_\theta(\boldsymbol{x})|]$ and $\mathbb{E}_{p(\boldsymbol{x})}[|\mathcal{F}\boldsymbol{s}_\theta(\boldsymbol{x})|]$ share the same minimum value (zero) and uniqueness conditions for the solution under NC.

3.2 STEADY-STATE DATA GENERATION

To evaluate the score loss, we need training data from the true distribution $p(\boldsymbol{x})$ of SFP equation, which can be sampled through the SDE simulation.

Dataset generation. Since the SDE is described by a steady-state equation, the stochastic system always reaches an invariant equilibrium distribution under the combined effects of drift and diffusion. Thus, we can freely choose the initial distribution $p_0(\boldsymbol{x})$ and sample an initial point set. These particles then evolve according to the SDE dynamics over a long time T[3] to produce a training dataset $\mathcal{D}_{\text{train}}$ from the target distribution $p \approx p_T$.

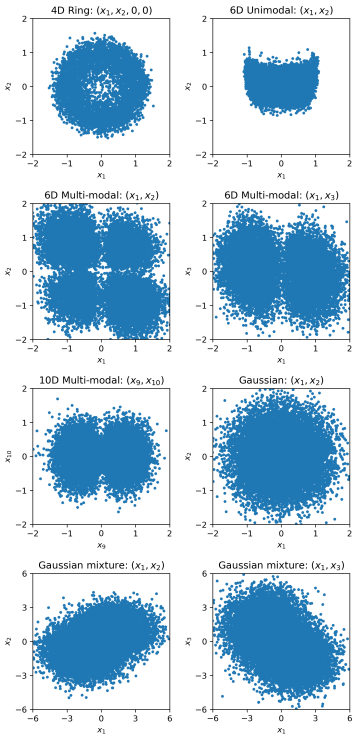

Algorithm 1 SRK method for steady-state data generation

Input: terminal time T, number of time steps N, initial distribution p_0, drift term $\boldsymbol{\mu}(\boldsymbol{x})$ and diffusion term $\boldsymbol{\sigma}(\boldsymbol{x})$
// Dataset generation phase
Select initial points $\boldsymbol{x}_0 \sim p_0$
Compute $\Delta t = T/N$
for $n = 0, 1, \ldots, N-1$ **do**
  Sample $\Delta \mathbf{W}_n \sim \mathcal{N}(0, \Delta t)$
  $\boldsymbol{\mu}_0 = \boldsymbol{\mu}(\boldsymbol{x}_n), \quad \boldsymbol{\sigma}_0 = \boldsymbol{\sigma}(\boldsymbol{x}_n)$
  $\boldsymbol{\sigma}_1 = \boldsymbol{\sigma}(\boldsymbol{x}_n + \boldsymbol{\sigma}_0 \Delta \mathbf{W}_n/2)$
  $\boldsymbol{\sigma}_2 = \boldsymbol{\sigma}(\boldsymbol{x}_n + \boldsymbol{\mu}_0(3\Delta t + \Delta \mathbf{W}_n^2)/4 + \boldsymbol{\sigma}_1 \Delta \mathbf{W}_n/2)$
  $\boldsymbol{\sigma}_3 = \boldsymbol{\sigma}(\boldsymbol{x}_n + \boldsymbol{\mu}_0(3\Delta t - \Delta \mathbf{W}_n^2)/2 + \boldsymbol{\sigma}_2 \Delta \mathbf{W}_n)$
  $\boldsymbol{\mu}_1 = \boldsymbol{\mu}(\boldsymbol{x}_n + \boldsymbol{\mu}_0(3\Delta t - \Delta \mathbf{W}_n^2)/2 + \boldsymbol{\sigma}_2 \Delta \mathbf{W}_n)$
  $\overline{\boldsymbol{\mu}} = (\boldsymbol{\mu}_0 + \boldsymbol{\mu}_1)/2$
  $\overline{\boldsymbol{\sigma}} = (\boldsymbol{\sigma}_0 + 2\boldsymbol{\sigma}_1 + 2\boldsymbol{\sigma}_2 + \boldsymbol{\sigma}_3)/6$
  $\boldsymbol{x}_{n+1} = \boldsymbol{x}_n + \overline{\boldsymbol{\mu}} \Delta t + \overline{\boldsymbol{\sigma}} \Delta \mathbf{W}_n$
end for
Generate training dataset $\mathcal{D}_{\text{train}} = \boldsymbol{x}_N \sim p_T$
// Domain selection phase
Find the spatial bounds $a_i = \min(x_i), b_i = \max(x_i)$ $(i = 1, \ldots, d)$ for $\boldsymbol{x} \in \mathcal{D}_{\text{train}}$
Determine the domain $\Omega = \bigotimes_{j=1}^{d} [a_i, b_i]$
Output: $\mathcal{D}_{\text{train}}, \Omega$

Figure 3: *Left*: Cross-sectional views of the training data distributions for SFP equations with complex patterns. *Right*: The SRK method consisting of two phases: dataset generation and domain selection.

Domain selection. Based on these samples, we determine an appropriate domain Ω for SFP problems, as the regions not covered by dataset $\mathcal{D}_{\text{train}}$ have very low or near-zero probability density. This implies that the integral of the true density function outside Ω (i.e., $1 - \int_\Omega p(\boldsymbol{x}) d\boldsymbol{x}$) is approximately zero. And this fact provides a theoretical guarantee for calculating the partition function Z_θ over Ω. Additionally, training FPNN on Ω conserves computational resources and avoids the undefined value of $\log \widetilde{p}_\theta(\boldsymbol{x})$ at $\widetilde{p}_\theta(\boldsymbol{x}) = 0$. There is no need to add gated functions or enforce BCs, because the correct score model will ensure that p_θ is close to 0 at $\partial\Omega$.

We use SRK methods for the strong approximation of SDE, and generate trajectories and samples with the strong order 1.5 Newton scheme (Newton, 1991). The training dataset $\mathcal{D}_{\text{train}}$ and problem domain Ω are adaptively provided by Algorithm 1. Other numerical approximations for SDE simulation are alternatives, such as the Euler-Maruyama method and the Milstein method (Bayram et al., 2018). For FPNN, we do not require the data points to exactly follow the true distribution $p(\boldsymbol{x})$, and our loss function offers a degree of tolerance and flexibility. The SRK method and its generated data for different SFP equations are given in Figure 3.

[3]Specifically, $\int_0^T |\boldsymbol{\mu}(\boldsymbol{x}(t))| dt$ needs to be sufficiently large to ensure that the particles thoroughly explore the spatial space and eventually reach a steady state.

3.3 NETWORK ARCHITECTURE

FPNN separates the score model learning from NC, allowing for unrestricted network architectures. In our implementation, we focus on two general approximators: TNN and MLP to model the unnormalized density $\widetilde{p}_\theta(\boldsymbol{x})$. The former is considered for its significant reduction in computational complexity when performing high-dimensional numerical integration for Z_θ. The latter is widely used in deep learning tasks and the integral over domain Ω can be estimated by Monte Carlo sampling. Both networks are modified to better accommodate complex SFP equations.

3.3.1 TENSOR NEURAL NETWORKS

Inspired by SPINN (Cho et al., 2024) and TNN (Wang et al., 2022), we parametrize each spatial component using an separated neural network $f_i : \mathbb{R} \to \mathbb{R}^r$, which takes the coordinates of i-th axis as input and produces a r-dimensional feature representation. We propose the power embedding (PE) to enhance the representation and better capture high-order drift dynamics. In each dimension, the input x_i is transformed into $[x_i, x_i^2, \cdots, x_i^m]$ before being fed into the network f_i (m is a manually specified hyper-parameter). This embedding enables the model to learn complex PDFs more efficiently and accurately (see Tables 4). The final prediction is obtained by taking an element-wise product of these r-dimensional features and summing the result:

$$\widetilde{p}_\theta(\boldsymbol{x}) = \sum_{j=1}^{r} \prod_{i=1}^{d} f_{i,j}(x_i; \theta_i) \tag{6}$$

We employ the activation function $tanh$ for all hidden layers and add an additional $softplus$ activation function before the output layer of the sub-networks f_i to make density $\widetilde{p}_\theta(\boldsymbol{x})$ strictly positive. A k-dimensional TNN can be built with k one-dimensional TNNs and approximate any k-dimensional vector functions $u : \mathbb{R}^d \to \mathbb{R}^k$. For details on the approximation properties, refer to Theorem 2.1 of TNN (Wang et al., 2022) and Appendix D.4 of SPINN (Cho et al., 2024).

Due to the low-rank structure of density representation in TNN, an efficient and accurate quadrature scheme can be designed for high-dimensional integration. Theorem 2 decomposes the high-dimensional integral of density $\widetilde{p}_\theta(\boldsymbol{x})$ into a series of one-dimensional integrals, and we efficiently compute it using the piece-wise Gauss-Legendre quadrature rule within 10 subintervals.

Theorem 2 (Partition function calculation)**.** *Given the density $\widetilde{p}_\theta(\boldsymbol{x})$ parameterized by TNN, the partition function Z_θ is computed as,*

$$Z_\theta \approx \sum_{j=1}^{r} \prod_{i=1}^{d} \left(\sum_{n_i=1}^{N_i} w_i^{(n_i)} f_{i,j}\left(x_i^{(n_i)}; \theta_i\right) \right) \tag{7}$$

where the nodes $\{x_i^{(n_i)}\}_{n_i=1}^{N_i}$ and weights $\{w_i^{(n_i)}\}_{n_i=1}^{N_i}$ are used for numerical integration in the i-th dimension ($i = 1, \ldots, d$).

3.3.2 MULTI-LAYER PERCEPTRON

To illustrate the applicability of our score PDE loss to different network architectures, we parameterize the d-dimensional spatial variables using an MLP $f_\theta : \mathbb{R}^d \to \mathbb{R}^r$. The $tanh$ function is used in hidden layers and the softplus function is employed to ensure non-negativity in the output layer. The r-dimensional features are summed up to produce the final output:

$$\widetilde{p}_\theta(\boldsymbol{x}) = \sum_{j=1}^{r} f_j(\boldsymbol{x}; \theta) \tag{8}$$

In our experiments, we find that hidden neurons with small activation values are overshadowed and inadequately trained in the original setup. And the modified MLP demonstrates improved learning performance.

Efficient numerical integration in Eq. (7) essentially forms high-dimensional grids using tensor products, which imposes certain requirements on the network architecture. More generally, we provide

the Monte Carlo estimation of partition function:

$$Z_\theta \approx \int_\Omega \widetilde{p}_\theta(\boldsymbol{x}) d\boldsymbol{x} = \mathbb{E}_{q(\boldsymbol{x})}\left[\frac{\widetilde{p}_\theta(\boldsymbol{x})}{q(\boldsymbol{x})}\right] \tag{9}$$

For simplicity, we set $q(\boldsymbol{x})$ as an uniform distribution on Ω, i.e., $q(\boldsymbol{x}) = \frac{1}{\nu(\Omega)}$ for $\boldsymbol{x} \in \Omega$, where ν denotes the Lebesgue measure. Since the optimization process does not involve normalization operations, we are free to choose the quadrature scheme to compute Z_θ by post-processing.

4 Experiment

Consider the challenges of solving high-dimensional SFP equations, we evaluate on several benchmark problems with analytical solutions. The 4D Ring is tested in FP solver (Zhai et al., 2022), while the 6D problems and 10D Multi-modal problem are adapted from TFFN (Wang et al., 2024). We further construct the 10D Gaussian mixture distribution (Tang et al., 2022) and 20D Gaussian function to comprehensively test the applicability of our FPNN. Our PDE examples span various 4-20 dimensional steady-state solutions, including ring-shape density, arbitrary potential function, and Gaussian mixture distribution, with complicated interactions among spatial coordinates.

Notably, few recent works can effectively solve such high-dimensional, challenging and different types of SFP equations, without the limitations in Table 1. We utilize TFNN as the baseline for comparison. The models are implemented in PyTorch framework and trained on NVIDIA Quadro RTX 8000 GPU with 48GB memory. Codes are provided in the supplementary material. We set a consistent seed across all experiments to ensure the reproducibility of our results.

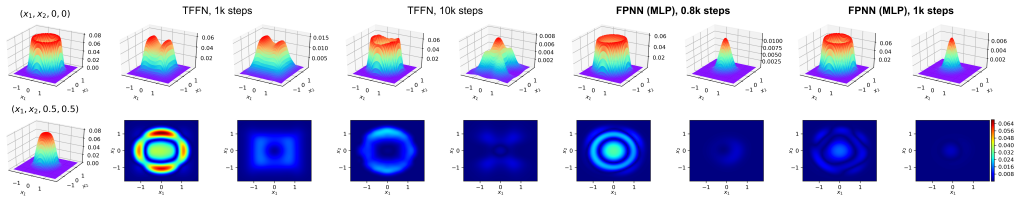

(a) 4D Ring

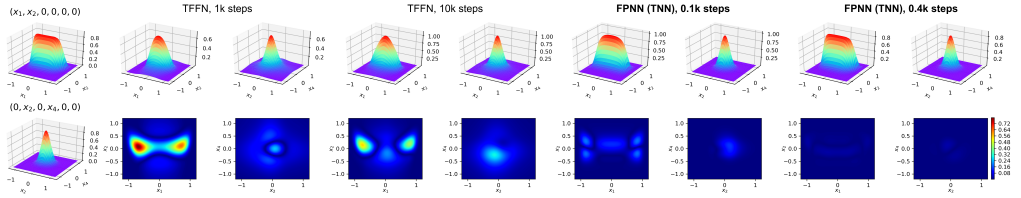

(b) 6D Unimodal

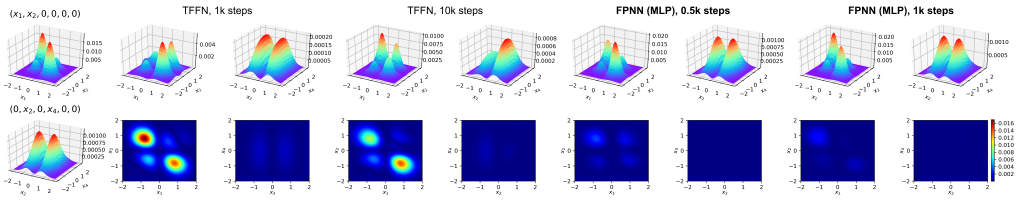

(c) 6D Multi-modal

Figure 4: Comparison of efficiency between TFFN and FPNN. The first column displays the true solution, while columns 2-5 and columns 6-9 show the predicted solutions (*top*) and corresponding MAE (*bottom*) for TFFN and FPNN during training. Both models utilize the same error colorbar for fair comparison.

4.1 Evaluation Metrics

Due to the small solutions to high-dimensional problems, mean absolute error (MAE) is insufficient to accurately evaluate the performance of models in different SFP problems. Even if the network learns a zero solution, MAE is not noticeable and merely equal the average true density on the test dataset, making it difficult to identify this error. However, mean absolute percentage error (MAPE) results in 100%, giving us a great indicator of performance. We incorporate MAPE to measure the consistency between the predicted and true solutions.

For high-dimensional problems, we are limited to visualizing the results using selected slices. However, only testing errors on cross-sectional data is insufficient to measure the performance of high-dimensional solutions due to their multi-modal complexity. Thus, we generate a test dataset $\mathcal{D}_{\text{test}} = \{p(\boldsymbol{x}) > \epsilon, \boldsymbol{x} \in \mathbb{R}^d\}$ to globally evaluate error metrics. To avoid the ineffective MAPE, $\mathcal{D}_{\text{test}}$ is generated by the gradient ascent method on analytical solutions, with a threshold ϵ to reject extremely small probability densities. This approach is more efficient than the traditional method of randomly sampling spatial points and filtering out those with densities below ϵ. The same test dataset and evaluation metrics are used for FPNN and TFFN, ensuring a fair comparison.

Table 2: Experimental results of TFFN and FPNN on 4-6 dimensional SFP equations.

SFP equations	Domain Ω	**TFFN**		**FPNN (Ours)**	
		MAE	MAPE	MAE	MAPE
4D Ring	$[-1.8, 1.8]^4$	3.61×10^{-3}	49.25%	5.56×10^{-4}	3.84%
6D Unimodal	$[-1.2, 1.2]^6$	4.00×10^{-2}	293%	1.48×10^{-3}	4.33%
6D Multi-modal	$[-2, 2]^6$	1.84×10^{-3}	92.90%	1.98×10^{-4}	12.18%

4.2 Experimental Analysis

Score PDE loss. Without the interference from NC, score loss significantly improves the optimization dynamics, enabling FPNN to quickly learn the correct scores and successfully capture the shape of PDF. This is crucial for the post-process of calculating normalizing constant and is a key factor in the success of our framework. In Figure 5, we plot the training loss $\mathcal{J}_{\text{score}}$ of FPNN for various SFP equations. Unlike the vanilla PINN, the magnitude of $\mathcal{J}_{\text{score}}$ hardly change with increasing dimensionality or decreasing solutions. The score PDE loss consistently remains within a stable range of 10^2 to 10^{-1}, demonstrating numerical stability across dimensions. Empirical evidence shows that when $\mathcal{J}_{\text{score}}$ falls below 1, FPNN generally learns the density function well. Thus, score loss also serves as an indicator of training progress and guides the network training regardless of dimensionality.

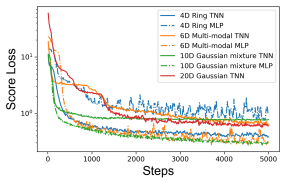

Figure 5: Plot of score PDE loss for 4-20 dimensional SFP equations during training.

Noting that both FPNN and TFFN strictly satisfy NC, we compare two PDE losses $\mathcal{J}_{\text{score}}$ and $\mathcal{J}_{\text{plain}}$ for 4D Ring problem in Figure 6. To balance the numerical scale of loss functions, we evaluate the plain PDE loss for FPNN and TFFN using $10k$ samples. These points are uniformly sampled from Ω and not used for training in both models. FPNN calculates Z_θ for normalization based on the current model at each step. Under the same evaluation, we observe that $\mathcal{J}_{\text{plain}}$ of FPNN drops faster and lower, indicating that our model trains more efficiently and stably using the score PDE loss. Moreover, although $\mathcal{J}_{\text{plain}}$ of TFFN also decreases to small values, the shape of approximate solution does not match the true density in Figure 4a. This deviation grows larger in higher-dimensional problems, leading to the failure or inapplicability of existing methods such as PINN and TFFN in high-dimensional SFP problems.

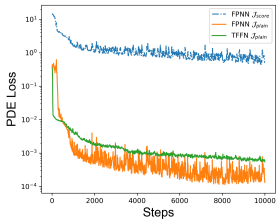

Figure 6: Plot of score PDE loss and plain PDE loss for 4D Ring.

Network Architecture. Increasing network capacity and width enhances model performance, resulting in fewer training steps and more accurate solutions. In Table 4 and Table 5, PE shows great

improvements in learning drift functions with high-order polynomial forms. Surprisingly, MLP-based FPNN utilizes 256 parameters to handle the complex 4D Ring problem and MAPE is reduced to 11.36% in only 4.8 minutes. In contrast, TFFN with 33,792 parameters is trained for 27.6 minutes and still fails to achieve comparable performance, as illustrated in Figure 4a. Given the flexibility in model, ResNet (He et al., 2016) is also alternative for deeper networks. In Figure 8, we observe that both TNN-based and MLP-based FPNN correctly capture the two peaks along the x_9 axis in 10D Multi-modal problem, requiring only 200 and $1k$ steps, respectively.

Table 3: Comparison of network structure for FPNN on high-dimensional SFP equations.

SFP equations	Domain Ω	Model	Parameters	MAE	MAPE
10D Multi-modal	$[-1.2, 1.2]^{10}$	TNN	84,480	1.26×10^{-4}	32.00%
		MLP	13,184	6.53×10^{-5}	18.30%
10D Gaussian mixture	$[-5, 5]^{10}$	TNN	126,080	1.84×10^{-7}	24.50%
		MLP	1,480	1.16×10^{-7}	18.38%
20D Gaussian	$[-2, 2]^{20}$	TNN	252,160	1.22×10^{-8}	12.79%

Partition Function. For MLP-based FPNN, we employ Monte Carlo sampling to draw a dataset $\mathcal{D}_Z$ from the distribution $q(\boldsymbol{x})$ and estimate the partition function Z_θ in Eq.(9). The size of $\mathcal{D}_Z$, denoted by $|\mathcal{D}_Z|$, determines the accuracy of unbiased estimation of Z_θ, which improves as $|\mathcal{D}_Z|$ increases. Figure 7a illustrates how the number of MC samples affects the estimation of Z_θ, and subsequently, the prediction error of our solution.

Due to the randomness, errors fluctuates significantly with small dataset $\mathcal{D}_Z$, especially in the range $|\mathcal{D}_Z| = 5k \sim 20k$. As $|\mathcal{D}_Z|$ increases, the prediction stabilizes. Higher-dimensional densities require more samples to accurately estimate the partition function. For all SFP problems, we set $|\mathcal{D}_Z| = 20k$, which our experiments show is sufficient for the accuracy of FPNN. However, for 10D Gaussian mixture problem, the expanded domain resulted in a MAPE of 58.66% with this setting. After increasing $|\mathcal{D}_Z|$ to $100k$, we get better solution with a MAPE of 18.38%.

For TNN-based FPNN, we also compare the Gauss-Legendre quadrature scheme in Eq.(7) with the MC sampling method in Eq.(9). As shown in Figure 7b, with more samples in $\mathcal{D}_Z$, the MC estimation Z_{MC} gradually approaches the numerical integration Z_{GL} (the rightmost column), and MAPE steadily decreases. More comparisons and limitations are provided in Appendix B.

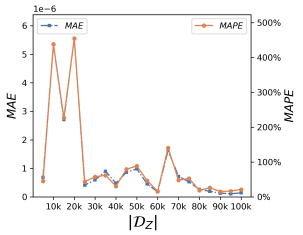

(a) MLP-based FPNN

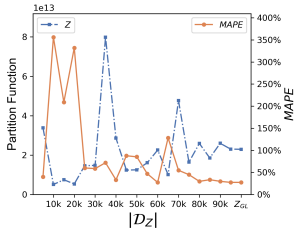

(b) TNN-based FPNN

Figure 7: 10D Gaussian mixture: MAE, MAPE and Z_θ at different $|\mathcal{D}_Z|$ for FPNN.

Model	Layers	Parameters	MAE	MAPE
TNN	[m, hidden layers, r]			
	[1, 64, 128]	33,792	7.27×10^{-3}	99.82%
	[3, 20, 20, 20, 20]	5,360	4.25×10^{-3}	65.41%
	[3, 64, 64, 64]	34,304	6.91×10^{-4}	7.58%
	[5, 64, 128]	34,816	8.20×10^{-4}	5.66%
	[8, 64, 128]	35,584	5.56×10^{-4}	3.84%
MLP	[d, hidden layers]			
	[4, 8, 8, 8, 8]	256	1.26×10^{-3}	11.36%
	[4, 20, 20, 20, 20]	1,360	9.74×10^{-4}	8.74%
	[4, 64, 64, 64]	8,640	8.81×10^{-4}	6.48%
	[4, 128, 128]	17,152	6.21×10^{-4}	5.39%

Table 4: 4D Ring: comparison of FPNN with different networks ($10k$ steps).

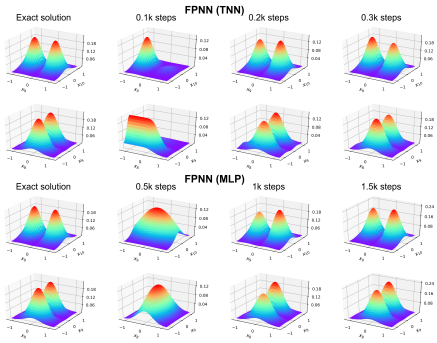

Figure 8: 10D Multi-modal: predicted solution of FPNN during training.

Model	Layers	Parameters	Steps	MAE	MAPE
TNN	[m, hidden layers, r]				
	[1, 20, 20, 20, 20]	7,800	$10k$	1.26×10^{-2}	30.60%
	[1, 64, 64, 64]	50,688	$2k$	1.33×10^{-2}	31.84%
	[3, 64, 64, 64]	51,456	$2k$	2.94×10^{-3}	9.49%
	[5, 64, 64, 64]	52,224	$2k$	2.44×10^{-3}	8.00%
	[8, 64, 128]	53,376	$2k$	2.18×10^{-3}	7.03%
	[8, 64, 128]	53,376	$10k$	1.48×10^{-3}	4.33%
MLP	[d, hidden layers]				
	[6, 8, 8, 8]	200	$4k$	2.46×10^{-2}	41.64%
	[6, 20, 20, 20]	980	$6k$	5.40×10^{-3}	13.87%
	[6, 64, 64, 64]	8,768	$10k$	2.94×10^{-3}	8.61%

Table 5: 6D Unimodal: comparison of FPNN with different networks.

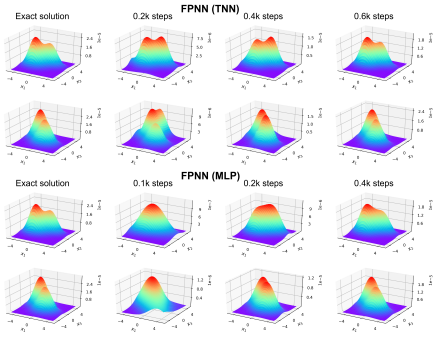

Figure 9: 10D Gaussian mixture: predicted solution of FPNN during training.

Computational Efficiency. Our computational complexity is significantly reduced compared to existing methods, because the normalization condition does not need to be explicitly considered during training. For PDE residuals, we only perform an additional logarithmic operation on the output layer, and the computational costs for $\mathcal{J}_{\text{plain}}$, $\mathcal{J}_{\text{score}}$ and their computational graphs remain roughly comparable. With the improved optimization dynamics and post-process of normalization, FPNN reduces both the total number of training epochs and the computational cost per iteration, achieving faster efficiency and enhanced performance.

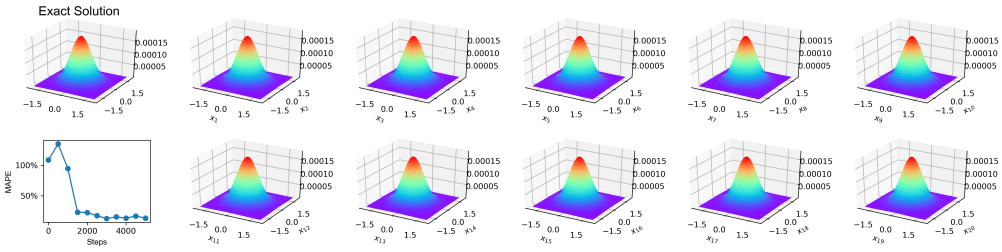

Figure 10: 20D Gaussian: predicted solution of FPNN. The first column shows the exact solution and the changes of MAPE during training. Due to symmetry, the cross-sections of any two dimensions near the origin exhibit the same shape. The remaining parts display the predicted densities for pairs of adjacent dimensions, such as $(x_1, x_2, 0, \ldots, 0)$, $(0, 0, x_3, x_4, 0, \ldots, 0)$, and so on.

5 Limitations and Future Work

Despite comprehensive experimental results show the effectiveness of our FPNN framework on challenging high-dimensional steady-state FP equations, there remain challenges on solving time-dependent FP equations. Time-varying probability densities are often non-localized and it is difficult to identify a suitable integration domain at any given time and compute the time-varying normalizing function. Our exploration is merely a promising start, and we look forward to its applications in broader fields, such as physics, finance, diffusion models, and mean-field games. In the future, we aim to extend the score-based FP loss to the time-dependent form and develop a flexible and efficient solver for general Fokker-Planck equations.

6 Conclusion

We propose a novel framework, FPNN, that decouples the normalization condition through score PDE loss for solving high-dimensional SFP equations. FPNN eliminates the computation and influence of the partition function for more efficient and stable training. In addition, arbitrary network architectures are allowed to strictly enforce normalization constraints, without sacrificing representation power. Our method outperforms existing methods in both training efficiency and prediction accuracy, demonstrating strong potential and general applicability.

REFERENCES

Ali Al-Aradi, Adolfo Correia, Gabriel Jardim, Danilo de Freitas Naiff, and Yuri Saporito. Extensions of the deep galerkin method. *Applied Mathematics and Computation*, 430:127287, 2022.

Hussam Alhussein, Mohammed Khasawneh, and Mohammed F Daqaq. Physics-informed solution of the stationary fokker-plank equation for a class of nonlinear dynamical systems: An evaluation study. *arXiv preprint arXiv:2309.16725*, 2023.

William Anderson and Mohammad Farazmand. Fisher information and shape-morphing modes for solving the fokker–planck equation in higher dimensions. *Applied Mathematics and Computation*, 467:128489, 2024.

Mustafa Bayram, Tugcem Partal, and Gulsen Orucova Buyukoz. Numerical methods for simulation of stochastic differential equations. *Advances in Difference Equations*, 2018:1–10, 2018.

Bruce M Boghosian, Adrian Devitt-Lee, Merek Johnson, Jie Li, Jeremy A Marcq, and Hongyan Wang. Oligarchy as a phase transition: The effect of wealth-attained advantage in a fokker–planck description of asset exchange. *Physica A: Statistical Mechanics and its Applications*, 476: 15–37, 2017.

Nan Chen and Andrew J Majda. Beating the curse of dimension with accurate statistics for the fokker–planck equation in complex turbulent systems. *Proceedings of the National Academy of Sciences*, 114(49):12864–12869, 2017.

Xiaoli Chen, Liu Yang, Jinqiao Duan, and George Em Karniadakis. Solving inverse stochastic problems from discrete particle observations using the fokker–planck equation and physics-informed neural networks. *SIAM Journal on Scientific Computing*, 43(3):B811–B830, 2021.

Junwoo Cho, Seungtae Nam, Hyunmo Yang, Seok-Bae Yun, Youngjoon Hong, and Eunbyung Park. Separable physics-informed neural networks. *Advances in Neural Information Processing Systems*, 36, 2024.

Yannick De Decker and Grégoire Nicolis. On the fokker–planck approach to the stochastic thermodynamics of reactive systems. *Physica A: Statistical Mechanics and its Applications*, 553:124269, 2020.

Laurent Dinh, Jascha Sohl-Dickstein, and Samy Bengio. Density estimation using real nvp. *arXiv preprint arXiv:1605.08803*, 2016.

Howard Elman, David Silvester, and Andy Wathen. *Finite elements and fast iterative solvers: with applications in incompressible fluid dynamics*. OUP Oxford, 2014.

Xiaodong Feng, Li Zeng, and Tao Zhou. Solving time dependent fokker-planck equations via temporal normalizing flow. *Communications in Computational Physics*, 32(2):401–423, 2022.

Jiequn Han, Arnulf Jentzen, and Weinan E. Solving high-dimensional partial differential equations using deep learning. *Proceedings of the National Academy of Sciences*, 115(34):8505–8510, 2018.

Kaiming He, Xiangyu Zhang, Shaoqing Ren, and Jian Sun. Deep residual learning for image recognition. In *Proceedings of the IEEE conference on computer vision and pattern recognition*, pp. 770–778, 2016.

Kurt Hornik, Maxwell Stinchcombe, and Halbert White. Multilayer feedforward networks are universal approximators. *Neural networks*, 2(5):359–366, 1989.

Jingwei Hu, JianGuo Liu, Yantong Xie, and Zhennan Zhou. A structure preserving numerical scheme for fokker-planck equations of neuron networks: Numerical analysis and exploration. *Journal of Computational Physics*, 433:110195, 2021.

Aapo Hyvärinen and Peter Dayan. Estimation of non-normalized statistical models by score matching. *Journal of Machine Learning Research*, 6(4), 2005.

Ziming Liu, Yixuan Wang, Sachin Vaidya, Fabian Ruehle, James Halverson, Marin Soljačić, Thomas Y Hou, and Max Tegmark. Kan: Kolmogorov-arnold networks. *arXiv preprint arXiv:2404.19756*, 2024.

Cheng Lu, Yuhao Zhou, Fan Bao, Jianfei Chen, Chongxuan Li, and Jun Zhu. Dpm-solver: A fast ode solver for diffusion probabilistic model sampling in around 10 steps. *Advances in Neural Information Processing Systems*, 35:5775–5787, 2022.

Calvin Luo. Understanding diffusion models: A unified perspective. *arXiv preprint arXiv:2208.11970*, 2022.

A Naess and V Moe. Efficient path integration methods for nonlinear dynamic systems. *Probabilistic engineering mechanics*, 15(2):221–231, 2000.

H Natarajan, PP Popov, and GB Jacobs. A high-order semi-lagrangian method for the consistent monte-carlo solution of stochastic lagrangian drift–diffusion models coupled with eulerian discontinuous spectral element method. *Computer Methods in Applied Mechanics and Engineering*, 384:114001, 2021.

Nigel J Newton. Asymptotically efficient runge-kutta methods for a class of ito and stratonovich equations. *SIAM Journal on Applied Mathematics*, 51(2):542–567, 1991.

Bernt Oksendal. *Stochastic differential equations: an introduction with applications*. Springer Science & Business Media, 2013.

Maziar Raissi, Paris Perdikaris, and George E Karniadakis. Physics-informed neural networks: A deep learning framework for solving forward and inverse problems involving nonlinear partial differential equations. *Journal of Computational Physics*, 378:686–707, 2019.

H Risken and TK Caugheyz. The fokker-planck equation: Methods of solution and application. *Journal of Applied Mechanics*, 58(3):860, 1991.

Justin Sirignano and Konstantinos Spiliopoulos. Dgm: A deep learning algorithm for solving partial differential equations. *Journal of computational physics*, 375:1339–1364, 2018.

Yang Song and Stefano Ermon. Improved techniques for training score-based generative models. *Advances in neural information processing systems*, 33:12438–12448, 2020.

Yang Song, Sahaj Garg, Jiaxin Shi, and Stefano Ermon. Sliced score matching: A scalable approach to density and score estimation. In *Uncertainty in Artificial Intelligence*, pp. 574–584. PMLR, 2020.

Yang Song, Jascha Sohl-Dickstein, Diederik P Kingma, Abhishek Kumar, Stefano Ermon, and Ben Poole. Score-based generative modeling through stochastic differential equations. In *International Conference on Learning Representations*, 2021.

Kejun Tang, Xiaoliang Wan, and Qifeng Liao. Adaptive deep density approximation for fokker-planck equations. *Journal of Computational Physics*, 457:111080, 2022.

Tongbi Tu, Ali Ercan, and M Levent Kavvas. Probabilistic solution to two-dimensional stochastic solute transport model by the fokker-planck equation approach. *Journal of Hydrology*, 580: 124250, 2020.

Taorui Wang, Zheyuan Hu, Kenji Kawaguchi, Zhongqiang Zhang, and George Em Karniadakis. Tensor neural networks for high-dimensional fokker-planck equations. *arXiv preprint arXiv:2404.05615*, 2024.

Yifan Wang, Pengzhan Jin, and Hehu Xie. Tensor neural network and its numerical integration. *arXiv preprint arXiv:2207.02754*, 2022.

Bing Yu et al. The deep ritz method: a deep learning-based numerical algorithm for solving variational problems. *Communications in Mathematics and Statistics*, 6(1):1–12, 2018.

Jiayu Zhai, Matthew Dobson, and Yao Li. A deep learning method for solving fokker-planck equations. In *Mathematical and scientific machine learning*, pp. 568–597. PMLR, 2022.

A LOSS FUNCTIONS FOR SFP EQUATIONS

We first introduce the loss functions and notations listed in Table 1 to provide the background for SFP equations. Then, we present the derivation of the score-based FP loss, which constitutes the core innovation and contribution of our work. Furthermore, we explain the relationship between the score PDE loss of SFP equations and the score-matching loss of generative models.

A.1 RELATED WORKS

PINN is a general deep-learning framework for solving PDEs and has achieved significant success in various problems, such as the Navier-Stokes equations, Allen-Cahn equation, Schrödinger equation, etc. However, PINN faces challenges in Fokker-Planck equations, with the plain PDE loss:

$$\mathcal{J}_{\text{plain}}(p_\theta) = \mathbb{E}\left[|\nabla \cdot (p_\theta \boldsymbol{\mu}) - \nabla \cdot (\nabla \cdot (D p_\theta))|\right] \tag{10}$$

It is evident that the zero solution $p_\theta = 0$ also satisfies this equation. Therefore, directly minimizing $\mathcal{J}_{\text{plain}}$ often leads to network collapse, where p_θ converges to a trivial solution. Data-driven methods rely on reference solutions $\{(\boldsymbol{x}_j, p_j)\}_{j=1}^N$ and introduce the regression loss:

$$\mathcal{J}_{\text{label}} = \frac{1}{N}\sum_{j=1}^{N}(p_\theta(\boldsymbol{x}_j) - p_j)^2 \tag{11}$$

Without labeled data, existing strategies generally fall into two categories involving normalization constraints in soft or hard manner. Soft constraints add a normalization penalty term to enforce $Z_\theta = 1$, thereby enabling the use of Eq.(9). This involves sampling a dataset $\mathcal{D}_{\text{norm}}$ from the distribution $q(\boldsymbol{x})$, with the number of samples given by $|\mathcal{D}_{\text{norm}}|$. In our experiments, $\Omega = \bigotimes_{j=1}^d [a_i, b_i]$ is a hypercube with the volume of $\nu(\Omega) = \prod_{i=1}^d |b_i - a_i|$. The normalization loss is defined as:

$$\mathcal{J}_{\text{norm}} = \left(\frac{\nu(\Omega)}{|\mathcal{D}_{\text{norm}}|}\sum_{\boldsymbol{x}\in\mathcal{D}_{\text{norm}}} p_\theta(\boldsymbol{x}) - 1\right)^2 \tag{12}$$

Hard constraints, on the other hand, develop specific structures to represent the density function, such as normalizing flows and their variants. The flow-based generative modeling is to seek an invertible mapping $\boldsymbol{z} = f(\boldsymbol{x})$ and the PDF of $\boldsymbol{x}$ follows the change of variables formula to strictly adhere NC.

$$p_X(\boldsymbol{x}) = p_Z(\boldsymbol{z})|\det \nabla_{\boldsymbol{x}} f(\boldsymbol{x})| \tag{13}$$

However, the former method requires manual balancing of multi-objective losses, while the latter may constrain the model's representation capacity. Furthermore, in terms of computational efficiency, TFFN requires estimating Z_θ at every iteration, "soft" PINN necessitates computing $\mathcal{J}_{\text{norm}}$ at each step, and density estimation with normalizing flows involves simultaneous tracking the changes of both x and log-density.

FPNN deviates from all existing approaches by changing the loss function directly. Our score PDE loss allows to model the unnormalized density $\widetilde{p}_\theta$ and decouples NC from the training process. Specifically, we replace $\mathcal{J}_{\text{plain}}$ with the following score PDE loss:

$$\begin{aligned} \mathcal{J}_{\text{score}}(\boldsymbol{s}_\theta) &= \mathbb{E}\left[|\nabla \log \widetilde{p}_\theta \cdot \widetilde{\boldsymbol{\mu}}(\boldsymbol{x}) + \nabla \cdot \widetilde{\boldsymbol{\mu}}(\boldsymbol{x})|\right], \\ \widetilde{\boldsymbol{\mu}}(\boldsymbol{x}) &= \boldsymbol{\mu}(\boldsymbol{x}) - \nabla \cdot D(\boldsymbol{x}) - D(\boldsymbol{x})\nabla \log \widetilde{p}_\theta \end{aligned} \tag{14}$$

In this form, the trivial solution $\widetilde{p}_\theta = 0$ no longer satisfies the equation. The score PDE loss maintains equivalence with the plain PDE loss while avoiding a zero solution and circumventing $\mathcal{J}_{\text{label}}$, $\mathcal{J}_{\text{norm}}$, or the normalization condition in loss function which causes difficulty in training.

A.2 DERIVATION OF SCORE PDE LOSS

Theorem 1 (Score-based FP loss)**.** *Assume the approximate solution $p_\theta(\boldsymbol{x})$ is differentiable and positive, satisfying regularity conditions: for a fixed set of $(\boldsymbol{\mu}(\boldsymbol{x}), \boldsymbol{D}(\boldsymbol{x}))$, $\mathbb{E}[|\mathcal{L}p_\theta(\boldsymbol{x})|]$ is finite for any θ. Denote the model score function as $\boldsymbol{s}_\theta(\boldsymbol{x}) := \nabla \log \widetilde{p}_\theta(\boldsymbol{x})$ to approximate $\nabla \log p(\boldsymbol{x})$ and*

$p(\boldsymbol{x})$ is the true solution of SFP equation. The plain PDE loss can be expressed as the following up to a constant factor

$$\mathbb{E}_{p(\boldsymbol{x})}[|\mathcal{F}\boldsymbol{s}_\theta(\boldsymbol{x})|] := \mathbb{E}_{\boldsymbol{x}\sim p(\boldsymbol{x})}[|\boldsymbol{s}_\theta(\boldsymbol{x})\cdot\widetilde{\boldsymbol{\mu}}(\boldsymbol{x}) + \nabla\cdot\widetilde{\boldsymbol{\mu}}(\boldsymbol{x})|] \tag{15}$$

where $\widetilde{\boldsymbol{\mu}}(\boldsymbol{x}) := \boldsymbol{\mu}(\boldsymbol{x}) - \nabla\cdot\boldsymbol{D}(\boldsymbol{x}) - \boldsymbol{D}(\boldsymbol{x})\boldsymbol{s}_\theta(\boldsymbol{x})$ does not explicitly involve the density. $\mathcal{F}$ is named as the score-based FP operator, and the proposed PDE loss solely depends on the score $\boldsymbol{s}_\theta(\boldsymbol{x})$.

Proof. First, for any positive probability density $p(\boldsymbol{x})$, note that $\mathcal{L}p(\boldsymbol{x})$ can be expanded to

$$\begin{aligned}
\mathcal{L}p(\boldsymbol{x}) &= -\nabla\cdot(p(\boldsymbol{x})\boldsymbol{\mu}(\boldsymbol{x})) + \nabla\cdot[\nabla\cdot(\boldsymbol{D}(\boldsymbol{x})p(\boldsymbol{x}))] \\
&= -\nabla\cdot(p(\boldsymbol{x})\boldsymbol{\mu}(\boldsymbol{x}) - \nabla\cdot(\boldsymbol{D}(\boldsymbol{x})p(\boldsymbol{x}))) \\
&= -\nabla\cdot(p(\boldsymbol{x})\boldsymbol{\mu}(\boldsymbol{x}) - (\nabla\cdot\boldsymbol{D}(\boldsymbol{x}))p(\boldsymbol{x}) - \boldsymbol{D}(\boldsymbol{x})\nabla p(\boldsymbol{x})) \\
&= -\nabla\cdot(p(\boldsymbol{x})(\boldsymbol{\mu}(\boldsymbol{x}) - \nabla\cdot\boldsymbol{D}(\boldsymbol{x}) - \boldsymbol{D}(\boldsymbol{x})\nabla\log p(\boldsymbol{x}))) \\
&= -\nabla\cdot(p(\boldsymbol{x})\widetilde{\boldsymbol{\mu}}(\boldsymbol{x})) \qquad (16)\\
&\overset{i.e.}{=} -\sum_{i=1}^{d}\frac{\partial}{\partial x_i}[p(\boldsymbol{x})\widetilde{\mu}_i(\boldsymbol{x})]
\end{aligned}$$

where we define

$$\widetilde{\boldsymbol{\mu}}(\boldsymbol{x}) := \boldsymbol{\mu}(\boldsymbol{x}) - \nabla\cdot\boldsymbol{D}(\boldsymbol{x}) - \boldsymbol{D}(\boldsymbol{x})\nabla\log p(\boldsymbol{x}) \tag{17}$$

For an approximate solution $p_\theta(\boldsymbol{x})$, the plain FP loss measures the expectation of PDE residuals $\mathcal{J}_{\text{plain}} = \mathbb{E}_{q(\boldsymbol{x})}[|\mathcal{L}p_\theta(\boldsymbol{x})|]$, where $q(\boldsymbol{x})$ can be selected as the uniform distribution on Ω. Based on Eq.(16), we can rewrite this loss to obtain

$$\begin{aligned}
\mathcal{J}_{\text{plain}}(p_\theta) = \mathbb{E}_{q(\boldsymbol{x})}[|\mathcal{L}p_\theta(\boldsymbol{x})|] &= \int_\Omega \frac{1}{\nu(\Omega)}|\mathcal{L}p_\theta(\boldsymbol{x})|d\boldsymbol{x} \qquad (18)\\
&= \frac{1}{\nu(\Omega)}\int_\Omega |\nabla p_\theta(\boldsymbol{x})\cdot\widetilde{\boldsymbol{\mu}}(\boldsymbol{x}) + p_\theta(\boldsymbol{x})(\nabla\cdot\widetilde{\boldsymbol{\mu}}(\boldsymbol{x}))|d\boldsymbol{x} \\
&= \frac{1}{\nu(\Omega)}\int_\Omega p_\theta(\boldsymbol{x})|\nabla\log p_\theta(\boldsymbol{x})\cdot\widetilde{\boldsymbol{\mu}}(\boldsymbol{x}) + \nabla\cdot\widetilde{\boldsymbol{\mu}}(\boldsymbol{x})|d\boldsymbol{x} \\
&= \frac{1}{\nu(\Omega)}\mathbb{E}_{p_\theta(\boldsymbol{x})}[|\nabla\log p_\theta(\boldsymbol{x})\cdot\widetilde{\boldsymbol{\mu}}(\boldsymbol{x}) + \nabla\cdot\widetilde{\boldsymbol{\mu}}(\boldsymbol{x})|] \\
&\approx \frac{1}{\nu(\Omega)}\mathbb{E}_{p(\boldsymbol{x})}[|\mathcal{F}\boldsymbol{s}_\theta(\boldsymbol{x})|] \\
&= \frac{1}{\nu(\Omega)}\mathcal{J}_{\text{score}}(\boldsymbol{s}_\theta) \qquad (19)
\end{aligned}$$

Our goal is to approximate the solution $p(\boldsymbol{x})$ and score $\nabla\log p(\boldsymbol{x})$ using $p_\theta(\boldsymbol{x})$ and $\boldsymbol{s}_\theta(\boldsymbol{x})$. Thus, we replace the expectation of p_θ with the ground truth p, allowing us to train the score model better. For SFP equations, we easily obtain samples from the invariant distribution $p(\boldsymbol{x})$ through SDE simulation. When p_θ is close to p, we observe that, up to a constant factor of $1/\nu(\Omega)$, the score-based FP loss is equivalent to the plain FP loss of PINN. But this form circumvents the need to handle the partition function and normalization condition. □

If we sample training data over a large spatial domain without prior knowledge, regions with extremely low density may fall below machine precision, resulting in $p_\theta = 0$ and "Not a Number" (NaN) errors for $\log p_\theta$. But it has no impact on the prediction stage, as there is no logarithmic operation. By using the SRK method to generate high-probability training data of the steady-state distribution, we define the domain of SFP problems and avoid this issue.

Sometimes, we can enhance training by adding weights $w(\boldsymbol{x})$ according to the probability density, and generalize the objective function as $\mathbb{E}_{p(\boldsymbol{x})}[|\mathcal{F}\boldsymbol{s}_\theta(\boldsymbol{x})|^\alpha], (0 < \alpha \leq 1)$. We set $\alpha = 1$ in our experiments, i.e., ℓ_1 norm for score loss function. Here is the following derivation:

$$\mathbb{E}_{p(\boldsymbol{x})}[|\mathcal{F}\boldsymbol{s}_\theta(\boldsymbol{x})|^\alpha] = \int_\Omega p(\boldsymbol{x})|\mathcal{F}\boldsymbol{s}_\theta(\boldsymbol{x})|^\alpha d\boldsymbol{x}$$

$$
\begin{aligned}
&\approx \nu(\Omega) \int_{\Omega} \frac{1}{\nu(\Omega)} p(\boldsymbol{x})^{1-\alpha} [p_\theta(\boldsymbol{x})^{\alpha} |\mathcal{F}\boldsymbol{s}_\theta(\boldsymbol{x})|^{\alpha}] d\boldsymbol{x} \\
&= \nu(\Omega) \mathbb{E}_{q(\boldsymbol{x})} [p(\boldsymbol{x})^{1-\alpha} |\mathcal{L}p_\theta(\boldsymbol{x})|^{\alpha}] \\
&= \nu(\Omega) \mathbb{E}_{q(\boldsymbol{x})} [w(\boldsymbol{x}) |\mathcal{L}p_\theta(\boldsymbol{x})|^{\alpha}]
\end{aligned} \tag{20}
$$

A.3 Connection between score PDE loss and score matching

To illustrate this connection, we consider a special case where $D(\boldsymbol{x}) = I_d$. If minimizing the score loss $\mathcal{J}_{\text{score}}$ drives $\widetilde{\boldsymbol{\mu}}(\boldsymbol{x})$ to zero, the training process becomes equivalent to optimizing the objective function of flow matching:

$$
\mathbb{E}_{p_{\text{data}}} [\|\boldsymbol{\mu}(\boldsymbol{x}) - \nabla \log \widetilde{p}_\theta\|_2^2] \tag{21}
$$

Thus, FPNN inherently integrates score matching while preserving the original Fokker-Planck equation and corresponding physical laws.

In Song's work (Song et al., 2021), the Noise Conditional Score Network (NCSN) uses a weighted sum of denoising score matching objectives:

$$
\theta^* = \arg\min_\theta \sum_{i=1}^{N} \sigma_i^2 \mathbb{E}_{p_{\text{data}}(\boldsymbol{x})} \mathbb{E}_{p_{\sigma_i}(\widetilde{\boldsymbol{x}}|\boldsymbol{x})} [\|\boldsymbol{s}_\theta(\widetilde{\boldsymbol{x}}, \sigma_i) - \nabla_{\widetilde{\boldsymbol{x}}} \log p_{\sigma_i}(\widetilde{\boldsymbol{x}}|\boldsymbol{x})\|_2^2] \tag{22}
$$

and Denoising Diffusion Probabilistic Model (DDPM) leverages a re-weighted variant of the evidence lower bound (ELBO):

$$
\theta^* = \arg\min_\theta \sum_{i=1}^{N} (1-\alpha_i) \mathbb{E}_{p_{\text{data}}(\boldsymbol{x})} \mathbb{E}_{p_{\alpha_i}(\widetilde{\boldsymbol{x}}|\boldsymbol{x})} [\|\boldsymbol{s}_\theta(\widetilde{\boldsymbol{x}}, i) - \nabla_{\widetilde{\boldsymbol{x}}} \log p_{\alpha_i}(\widetilde{\boldsymbol{x}}|\boldsymbol{x})\|_2^2] \tag{23}
$$

It can be seen that our equivalent score-matching loss:

$$
\theta^* = \arg\min_\theta \mathbb{E}_{p_{\text{data}}(\boldsymbol{x})} [\|\boldsymbol{s}_\theta(\boldsymbol{x}) - \boldsymbol{\mu}(\boldsymbol{x})\|_2^2] \tag{24}
$$

shares a similar form with score-based generative models. These generative models gradually learn the "score" of the perturbed data distribution (i.e., conditional Gaussian distribution), while our FPNN directly learns the known drift $\boldsymbol{\mu}(\boldsymbol{x})$ for solving FP equations.

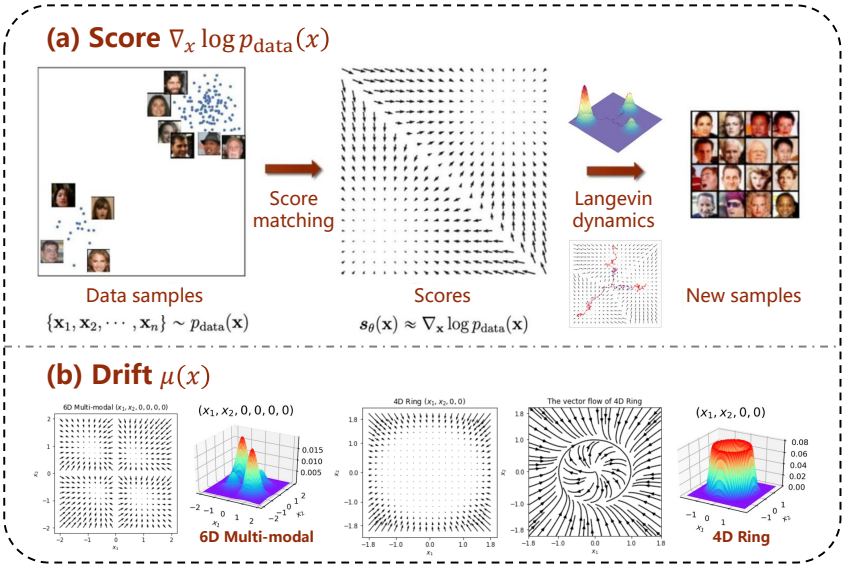

Figure 11: (a) the score in generative models and (b) the drift in SFP equations. Both represent gradient information of the data distribution and indicate regions of high probability.

We further demonstrate the relationship between "drift" and "score". Both are vector fields in high-dimensional spaces that indicate the direction of high-density sampling. The distinction lies in their domains: the drift function here operates in the physical space, whereas the score is typically defined in image or feature space and lacks an analytical form.

B COMPUTATION OF PARTITION FUNCTION

The main proof is derived from Section 3 of Wang et al. (2022). Here, we demonstrate the simplified integral expression relevant to our work, and the conclusion remains valid for the power embedding.

Theorem 2 (Partition function calculation)**.** *Given the density $\widetilde{p}_\theta(\boldsymbol{x})$ parameterized by TNN, the partition function Z_θ is computed as,*

$$Z_\theta \approx \sum_{j=1}^{r} \prod_{i=1}^{d} \left(\sum_{n_i=1}^{N_i} w_i^{(n_i)} f_{i,j}\left(x_i^{(n_i)}; \theta_i\right) \right) \tag{25}$$

where the nodes $\{x_i^{(n_i)}\}_{n_i=1}^{N_i}$ and weights $\{w_i^{(n_i)}\}_{n_i=1}^{N_i}$ are used for numerical integration in the i-th dimension ($i = 1, \ldots, d$).

Proof. For the unnormalized density $\widetilde{p}_\theta(\boldsymbol{x})$ represented by TNN, the computation of Z_θ can be decomposed into d one-dimensional integrals:

$$\begin{aligned}
Z_\theta &\approx \int_\Omega \widetilde{p}_\theta(\boldsymbol{x}) d\boldsymbol{x} \\
&= \int_\Omega \sum_{j=1}^{r} \prod_{i=1}^{d} f_{i,j}(x_i) d\boldsymbol{x} \\
&= \sum_{j=1}^{r} \int_\Omega \prod_{i=1}^{d} f_{i,j}(x_i) d\boldsymbol{x} \qquad (26) \\
&= \sum_{j=1}^{r} \int_{a_d}^{b_d} \cdots \int_{a_1}^{b_1} f_{1,j}(x_1) \cdots f_{d,j}(x_d) dx_1 \cdots dx_d \\
&= \sum_{j=1}^{r} \left(\int_{a_1}^{b_1} f_{1,j}(x_1) dx_1 \right) \cdots \left(\int_{a_d}^{b_d} f_{d,j}(x_d) dx_d \right) \qquad (27)
\end{aligned}$$

For simplicity, we omit the parameters θ_i in network f_i. Eq.(26) holds due to the linearity of integral and Eq.(27) follows the fact that the sub-network f_i solely depends only on x_i ($i = 1, \ldots, d$). Without loss of generality, for the i-th dimension, we use a piece-wise Gauss–Legendre quadrature rule to compute the one-dimensional integral $\int_{a_i}^{b_i} f_{i,j}(x_i) dx_i$ and then compute Z_θ in Eq.(27). Specifically, we select N_i Gauss points $\{x_i^{(n_i)}\}_{n_i=1}^{N_i}$ and corresponding weights $\{w_i^{(n_i)}\}_{n_i=1}^{N_i}$, introducing the index $n = (n_1, \cdots, n_d) \in \mathcal{N} := \{1, \ldots, N_1\} \times \cdots \times \{1, \ldots, N_d\}$. Hence, Gauss points and weights for numerical integration over the high-dimensional domain Ω are represented as:

$$\begin{aligned}
\{\boldsymbol{x}^{(n)}\}_{n \in \mathcal{N}} &= \left\{ (x_1, \cdots, x_d) | x_i = x_i^{(n_i)}, i = 1, \ldots, d \right\} \\
\{w^{(n)}\}_{n \in \mathcal{N}} &= \left\{ \prod_{i=1}^{d} w_i | w_i = w_i^{(n_i)}, i = 1, \ldots, d \right\}
\end{aligned} \tag{28}$$

The partition function is computed by numerical integration:

$$\begin{aligned}
Z_\theta &\approx \int_\Omega \widetilde{p}_\theta(\boldsymbol{x}) d\boldsymbol{x} \\
&\approx \sum_{n \in \mathcal{N}} w^{(n)} \widetilde{p}_\theta(\boldsymbol{x}^{(n)}) \\
&= \sum_{(n_1, \cdots, n_d) \in \mathcal{N}} w_1^{(n_1)} \cdots w_d^{(n_d)} \sum_{j=1}^{r} \prod_{i=1}^{d} f_{i,j}\left(x_i^{(n_i)}\right) \\
&= \sum_{j=1}^{r} \sum_{(n_1, \cdots, n_d) \in \mathcal{N}} \left(w_1^{(n_1)} f_{1,j}\left(x_1^{(n_1)}\right) \right) \cdots \left(w_d^{(n_d)} f_{d,j}\left(x_d^{(n_d)}\right) \right)
\end{aligned}$$

$$= \sum_{j=1}^{r} \left(\sum_{n_1=1}^{N_1} w_1^{(n_1)} f_{1,j}\left(x_1^{(n_1)}\right) \right) \cdots \left(\sum_{n_d=1}^{N_d} w_d^{(n_d)} f_{d,j}\left(x_d^{(n_d)}\right) \right) \tag{29}$$

□

Since the cost of each one-dimensional integral is independent of the dimensionality, the overall computational complexity for the high-dimensional integration is the linear scale of dimension d. And we only calculate the partition function once in FPNN.

The advantages and differences between two computations of Z_θ are summarized as follows:

- **MLP-based FPNN.** The advantages of MLP lie in simpler feature fusion of spatial variables and faster computation of partition functions Z_θ using MC sampling:

$$Z_\theta = \frac{\nu(\Omega)}{|\mathcal{D}_{\text{norm}}|} \sum_{\boldsymbol{x} \in \mathcal{D}_{\text{norm}}} \widetilde{p}_\theta(\boldsymbol{x}) \tag{30}$$

  However, in particularly high-dimensional settings or the large range of each interval in Ω, the volume of Ω, i.e., $\nu(\Omega) = \prod_{i=1}^{d} |b_i - a_i|$ may exceed machine limits. This issue can be addressed by narrowing the intervals of interest or using higher numerical precision, such as 'float64'.

- **TNN-based FPNN.** TNN achieves high precision in numerical integration for estimating Z_θ, making it more suitable for higher-dimensional problems. Unlike MLP, TNN can maintain appropriate values for the integral in each spatial dimension (i.e., $\int_{a_i}^{b_i} f_{i,j}(x_i) dx_i$), regardless of the dimensionality or the interval length. Introducing regularization terms to guide the learning of smaller unnormalized density is an effective strategy to alleviate the numerical difficulties associated with the partition function.

C Experimental details of PDEs

We remark that FPNN is adaptable to a wide range of SFP equations, but most problems are difficult to obtain analytical solutions for performance evaluation. Inspired by Wang et al. (2024), we use gradient systems to construct test PDE cases with exact solutions. Given any potential function $H(\boldsymbol{x})$ and diffusion term $\boldsymbol{\sigma}(\boldsymbol{x})$, we calculate the diffusion matrix $\boldsymbol{D}(\boldsymbol{x}) = \frac{1}{2}\boldsymbol{\sigma}(\boldsymbol{x})\boldsymbol{\sigma}(\boldsymbol{x})^T$ and set the drift term as follows:

$$\boldsymbol{\mu}(\boldsymbol{x}) = -\boldsymbol{D}(\boldsymbol{x})\nabla H(\boldsymbol{x}) + \nabla \cdot \boldsymbol{D}(\boldsymbol{x}) \tag{31}$$

Then the solution to the SFP equation $\mathcal{L}p(\boldsymbol{x}) = 0$ with respect to $(\boldsymbol{\mu}, \boldsymbol{D})$ reads

$$p(\boldsymbol{x}) = \frac{1}{Z} e^{-H(\boldsymbol{x})}, \qquad Z = \int e^{-H(\boldsymbol{x})} d\boldsymbol{x} \tag{32}$$

It can be easily verified that

$$\begin{aligned} \mathcal{L}p(\boldsymbol{x}) &= -\nabla \cdot (p(\boldsymbol{x})\boldsymbol{\mu}(\boldsymbol{x})) + \nabla \cdot [\nabla \cdot (\boldsymbol{D}(\boldsymbol{x})p(\boldsymbol{x}))] \\ &= \nabla \cdot (-p(\boldsymbol{x})\boldsymbol{\mu}(\boldsymbol{x}) + (\nabla \cdot \boldsymbol{D}(\boldsymbol{x}))p(\boldsymbol{x}) + \boldsymbol{D}(\boldsymbol{x})\nabla p(\boldsymbol{x})) \\ &= \nabla \cdot (-p(\boldsymbol{x})\boldsymbol{\mu}(\boldsymbol{x}) + (\nabla \cdot \boldsymbol{D}(\boldsymbol{x}))p(\boldsymbol{x}) - \boldsymbol{D}(\boldsymbol{x})\nabla H(\boldsymbol{x})p(\boldsymbol{x})) \\ &= 0 \end{aligned} \tag{33}$$

The stochastic system is given by $d\mathbf{X} = \boldsymbol{\mu}(\mathbf{X})dt + \boldsymbol{\sigma}(\mathbf{X})d\mathbf{W}_t$. We adopt this form to design SFP equations C.2-C.4. For exact solutions in our experiments, we use the *SymPy* library to compute the partition function in Eq.(32). *SymPy* is a powerful and versatile tool for symbolic mathematics and provides computer algebra system (CAS) capabilities directly in Python. We point out that appropriate simplifications (e.g., completing the square and variable substitution) and the choice of integration order significantly impact the accuracy of results.

In Table 6, we list the network settings used for plotting experimental results, where TNN and MLP represent the architectures in FPNN framework using score PDE loss.

Table 6: Network structure settings used for visualizing experimental results.

SFP equations	Model	Layers	Parameters	Steps
4D Ring	TFFN	4×[1, 64, 64, 64]	33,792	20k
	TNN	4×[8, 64, 128]	35,584	10k
	MLP	[4, 20, 20, 20, 20]	1,360	10k
6D Unimodal	TFFN	6×[1, 64, 64, 64]	50,688	20k
	TNN	6×[5, 64, 64, 64]	52,224	5k
	MLP	[6, 20, 20, 20]	980	20k
6D Multi-modal	TFFN	6×[1, 64, 64, 64]	50,688	20k
	TNN	6×[5, 64, 64, 64]	52,224	5k
	MLP	[6, 32, 32, 32]	2,336	5k
10D Multi-modal	TNN	10×[1, 64, 64, 64]	84,480	1k
	MLP	[10, 64, 64, 64, 64]	13,184	5k
Gaussian mixture	TNN	10×[1, 64, 64, 64, 64]	126,080	5k
	MLP	[10, 20, 20, 20, 20]	1,480	5k
Gaussian	TNN	20×[1, 64, 64, 64, 64]	252,160	3k

C.1 4D RING

Consider a stochastic gradient system in four dimensional state space from Zhai et al. (2022). The deterministic part is a gradient system plus a perpendicular rotation term $\boldsymbol{r}(\boldsymbol{x}) = [x_2, -x_1, 0, 0]^T$, where the potential function of the gradient flow is $H(\boldsymbol{x}) = 2(||\boldsymbol{x}||_2^2 - 1)^2$. We use the SFP equation (2) with the following drift $\boldsymbol{\mu}(\boldsymbol{x})$ and diffusion $\boldsymbol{D}$:

$$\boldsymbol{\mu}(\boldsymbol{x}) = -\nabla H(\boldsymbol{x}) + \boldsymbol{r}(\boldsymbol{x}), \qquad \boldsymbol{D} = \frac{\sigma^2}{2}\boldsymbol{I}_4, \qquad \boldsymbol{\sigma} = \sigma \boldsymbol{I}_4 \tag{34}$$

Since $\boldsymbol{r}(\boldsymbol{x})$ is orthogonal to the equipotential lines of $H(\boldsymbol{x})$, the rotation term does not change the invariant probability density function. The invariant probability measure has density function

$$p(\boldsymbol{x}) = \frac{1}{Z} e^{-H(\boldsymbol{x})/\sigma^2}, \qquad Z = \pi^2 \int_{-1}^{\infty} (t+1) e^{-2t^2/\sigma^2} dt \tag{35}$$

Here, we utilize the polar coordinates, variable substitution, and the surface area formula of a 4D hypersphere $S = 2\pi^2 r^3$. We set $\sigma = 1$ and calculate the infinite integral for Z using *SymPy* library.

We generated a training dataset $\mathcal{D}_{\text{train}}$ with 20k samples using the 1.5-order SRK method, setting the terminal time $T = 1$, the number of time steps $N = 500$ and a 4-dimensional standard Gaussian distribution $p_0(\boldsymbol{x})$. Based on the range of the dataset $\mathcal{D}_{\text{train}}$, the domain is selected as $\Omega = [-1.8, 1.8]^4$.

For the test dataset generation, we sample 10k initial points uniformly within Ω. Then we perform the gradient ascent using the true solution $p(\boldsymbol{x})$, with a learning rate of 1×10^{-3} and the threshold $\epsilon = 1 \times 10^{-3}$. For fair comparison, we use the same test dataset D_{test} for TFNN and FPNN with TNN/MLP architectures.

For all SFP equations in our experiments, FPNNs are trained under consistent settings: we use Adam optimizer with a learning rate of 0.01 and a batch size of 2k, resulting in 10 iterations per epoch. The network structure and prediction performance are detailed in Table 4. TFFN consists of four sub-networks of 3 hidden layers with 64 hidden feature size, updated for 20k steps using the Adam optimizer with a learning rate of 0.01, as shown in Table 6. Training data are uniformly sampled from Ω, with 2k points resampled per iteration.

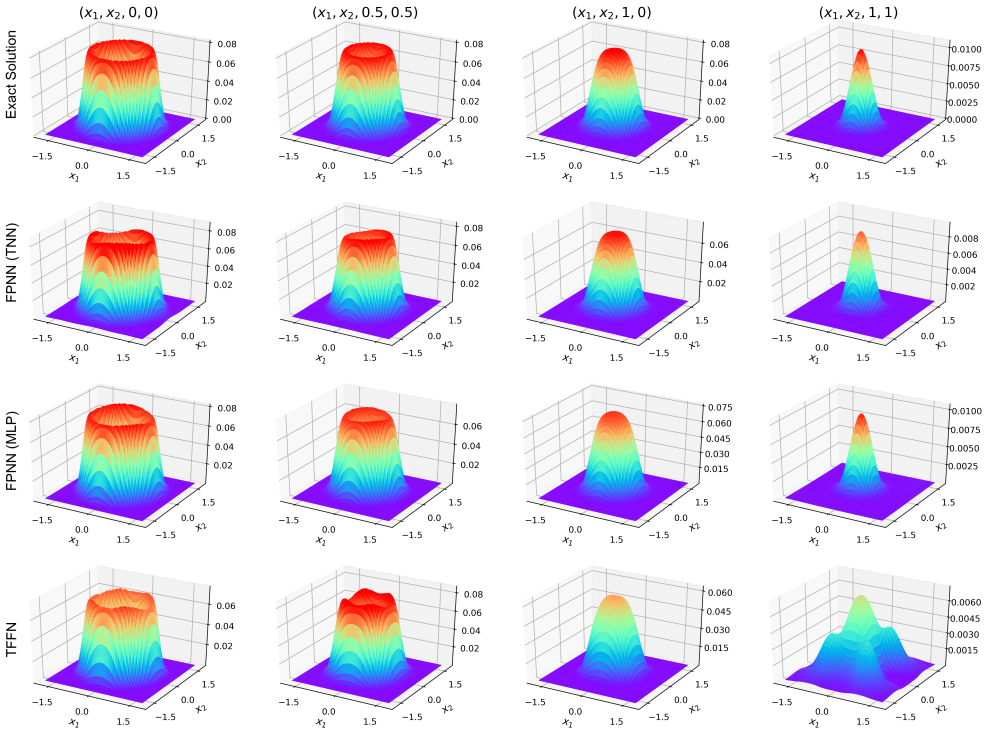

Figure 12: 4D Ring: the exact solution and predicted solutions of different models. First row: the exact solution. Second row: TNN-based FPNN. Third row: MLP-based FPNN. Last row: TFFN.

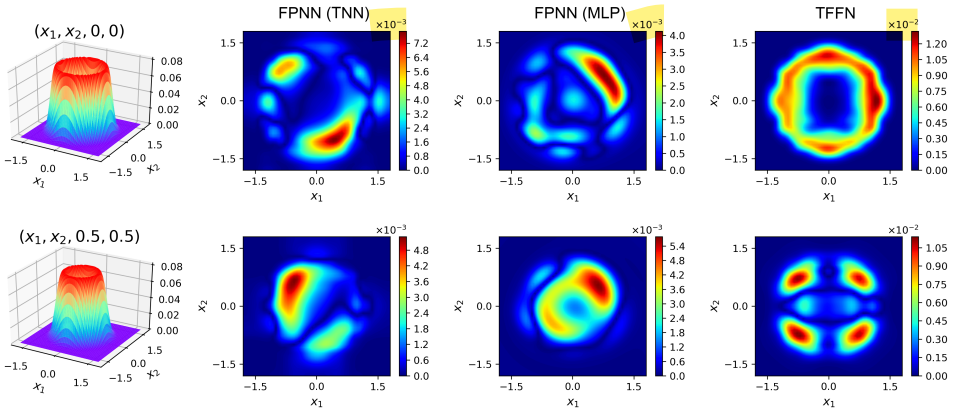

Figure 13: 4D Ring: MAE between the exact solution and predicted solutions of different models. First column: the exact solution. Second column: TNN-based FPNN. Third column: MLP-based FPNN. Last column: TFFN.

C.2 6D Unimodal

In this case, the diffusion $\boldsymbol{D} = \boldsymbol{I}_6$ and the drift $\boldsymbol{\mu}(\boldsymbol{x}) = -\nabla H(\boldsymbol{x})$ take the form in Eq.(31), where the potential function $H(\boldsymbol{x})$ is written as:

$$H(\boldsymbol{x}) = 3((x_1^4 - x_2)^2 + 2x_2^2 + (x_3^4 - x_4)^2 + 2x_4^2 + (x_5^4 - x_6)^2 + 2x_6^2) \tag{36}$$

The variables (x_1, x_2), (x_3, x_4), and (x_5, x_6) have distinct interactions in the form of $(x_i^4 - x_{i+1})^2 + 2x_{i+1}^2, i = 1, 3, 5$. The specific term results in $\boldsymbol{\mu}(\boldsymbol{x})$ being a polynomial function of degree up to 7, introducing significant nonlinearity and challenges for training model. Our proposed PE is inspired

by this complexity, and the goal is to alleviate the difficulty of fitting such high-order functions. The density function is more concentrated with steep gradients, and decays rapidly away from the origin. Although the density is unimodal, it remains a challenging problem for solving this SFP equation.

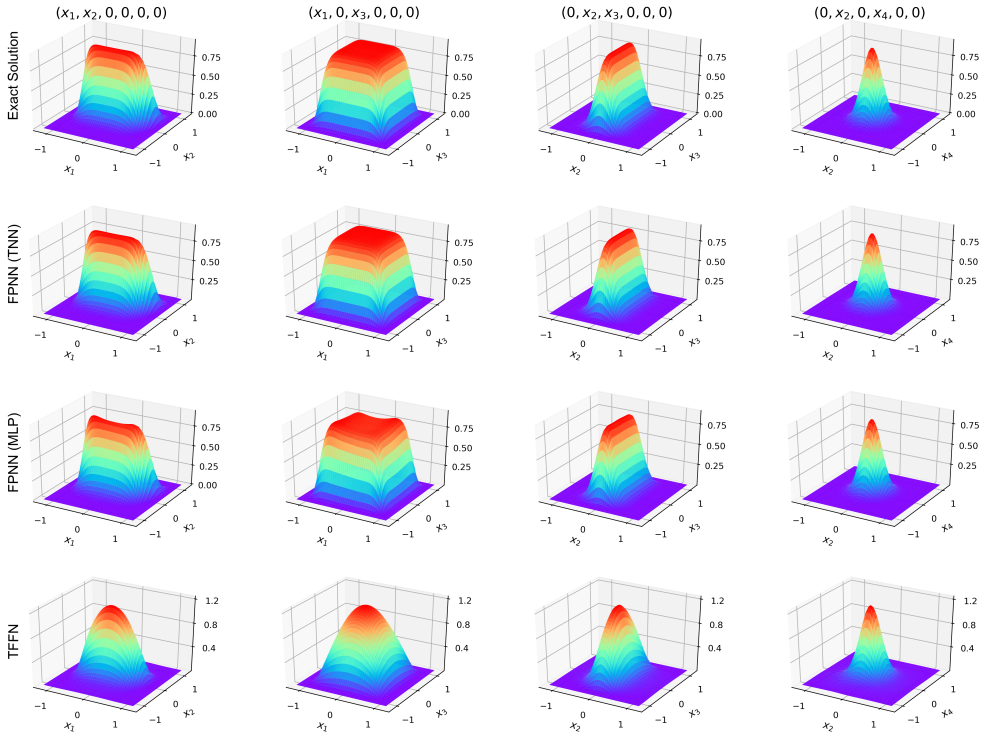

Figure 14: 6D Unimodal: the exact solution and predicted solutions of different models. First row: the exact solution. Second row: TNN-based FPNN. Third row: MLP-based FPNN. Last row: TFFN.

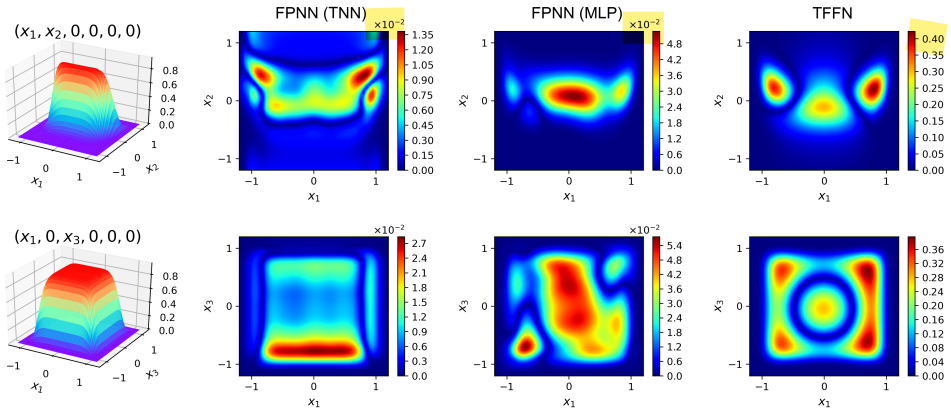

Figure 15: 6D Unimodal: MAE between the exact solution and predicted solutions of different models. First column: the exact solution. Second column: TNN-based FPNN. Third column: MLP-based FPNN. Last column: TFFN.

We set the terminal time $T = 1$ and the number of time steps $N = 500$. The initial distribution is a 6-dimensional Gaussian distribution with zero mean and covariance matrix $0.01\boldsymbol{I}_6$. And we generate $20k$ training points and select the domain $\Omega = [-1.2, 1.2]^6$. The test dataset is created by applying gradient ascent to $10k$ initial points from uniform distribution within Ω, with a learning rate of 1×10^{-3} and a threshold $\epsilon = 1\times10^{-5}$. We use the same training settings for FPNN, and comparisons

of different network architectures are shown in Table 5. Notably, PE significantly accelerates the learning of higher-order densities for TNNs. With appropriate embedding size m, TNN achieves MAPE below 10% with fewer steps, while MLP demonstrates its advantage by solving the 6D Unimodal problem with only 980 parameters.

C.3 6D MULTI-MODAL

We consider the potential $H(\boldsymbol{x})$ with a quadratic form, where the SFP equation is given by the diffusion $\boldsymbol{D} = \boldsymbol{I}_6$ and the drift $\boldsymbol{\mu}(\boldsymbol{x}) = -\nabla H(\boldsymbol{x})$ in Eq.(31). $H(\boldsymbol{x})$ involves interactions among (x_1, x_2, x_3) and (x_4, x_5, x_6), which possesses the following form:

$$\begin{aligned} H(\boldsymbol{x}) =& 2(x_1^2 + x_2^2 + x_3^2 + 0.5(x_1x_2 + x_1x_3 + x_2x_3)) - \ln(x_1^2 + 0.02) \\ & - \ln(x_2^2 + 0.02) + 0.5(x_4^2 + x_5^2 + x_6^2 + 0.2(x_4x_5 + x_4x_6 + x_5x_6)) \end{aligned} \tag{37}$$

The density function has four modes and we plot the slices of high-density regions from different dimensions to illustrate the performance.

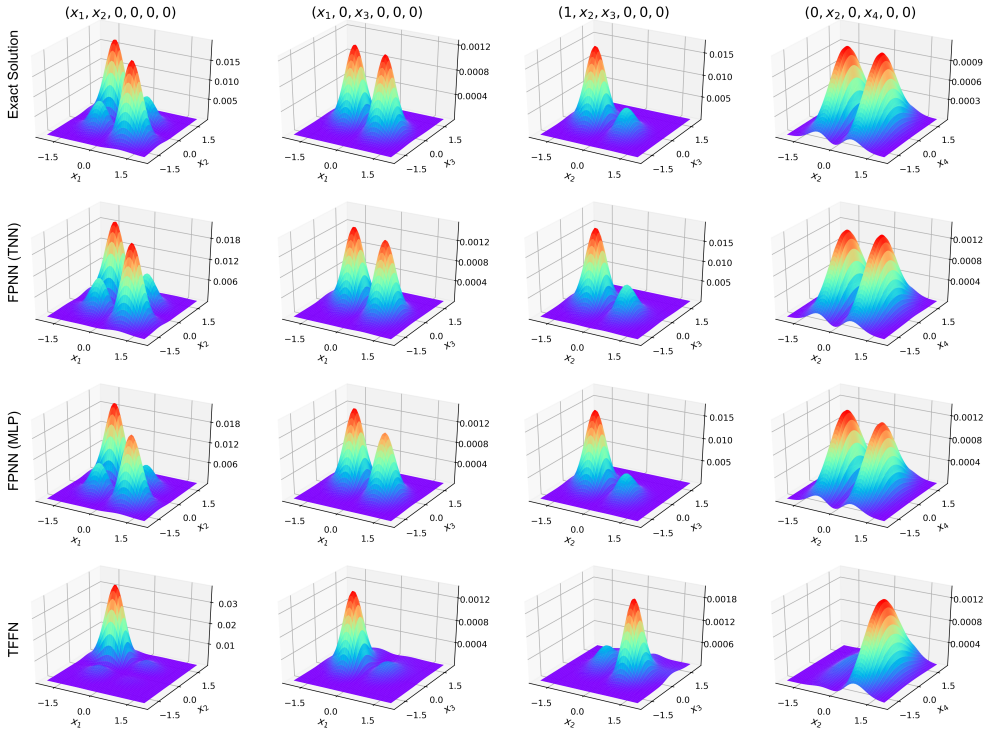

Figure 16: 6D Multi-modal: the exact solution and predicted solutions of different models. First row: the exact solution. Second row: TNN-based FPNN. Third row: MLP-based FPNN. Last row: TFFN.

We set the terminal time $T = 1$ and the number of time steps $N = 200$. The initial distribution is a 6-dimensional Gaussian distribution with zero mean and covariance matrix $0.1\boldsymbol{I}_6$. We generate $20k$ training points and determine domain $\Omega = [-2, 2]^6$ for 6D Multi-modal problem. We use a a learning rate of 1×10^{-3} and a threshold $\epsilon = 1 \times 10^{-5}$ to generate the test dataset with $10k$ samples by gradient ascent method.

From the numerical results in Table 7, MLP outperforms TNN in terms of parameter efficiency, training speed and prediction accuracy, achieving a MAPE of 12%. This may be attributed to the architectural characteristics of TNNs, which is more suitable for the solutions align with the variable separation form and quickly learns discrete low-rank features (see Table 5). Conversely, MLP is better at fusing features across spatial coordinates in hidden layers. FPNN allows the use of free-form network architectures, providing greater flexibility in handling SFP equations with diverse characteristics.

Table 7: 6D Multi-modal: comparison of FPNN with different networks (5k steps).

Model	Layers	Parameters	MAE	MAPE
TNN	[m, hidden layers, r]			
	[1, 64, 64, 64]	50,688	4.20×10^{-4}	35.76%
	[5, 64, 64, 64]	52,224	3.25×10^{-4}	23.11%
	[8, 64, 128]	53,376	2.30×10^{-4}	21.59%
MLP	[d, hidden layers]			
	[6, 20, 20, 20]	980	2.00×10^{-4}	12.72%
	[6, 32, 32, 32]	2,336	2.05×10^{-4}	12.72%
	[6, 64, 64]	4,608	1.98×10^{-4}	12.18%

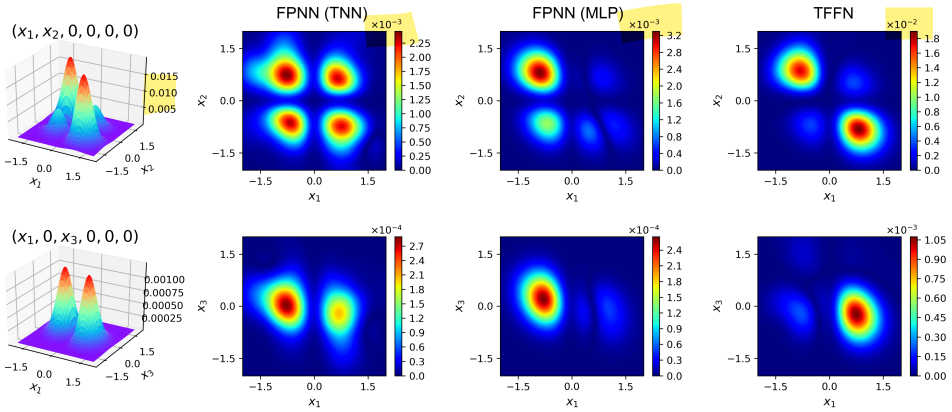

Figure 17: 6D Multi-modal: MAE between the exact solution and predicted solutions of different models. First column: the exact solution. Second column: TNN-based FPNN. Third column: MLP-based FPNN. Last column: TFFN.

C.4 10D Multi-modal

To evaluate the performance in high dimensions, we conduct experiments using a 10-dimensional probability density function with two modes. The SFP equation has the diffusion $\boldsymbol{D} = \boldsymbol{I}_{10}$, and the potential function $H(\boldsymbol{x})$ for the drift $\boldsymbol{\mu}(\boldsymbol{x})$ as follows:

$$H(\boldsymbol{x}) = 2.5(x_1^2 + x_2^2 + x_3^2 + 0.1(x_1x_2 + x_1x_3 + x_2x_3)) + 2(x_4^2 + x_5^2 + x_6^2 + 0.2(x_4x_5 + x_4x_6 + x_5x_6)) + 3(x_7^2 + x_8^2 - 0.01x_7x_8)) + 3(x_9^2 + x_{10}^2 - 0.01x_9x_{10})) - \ln(2x_9^2 + 0.02) \tag{38}$$

Here, $H(\boldsymbol{x})$ exhibits complex interactions across the coordinates (x_1, x_2, x_3), (x_4, x_5, x_6), (x_7, x_8) and (x_9, x_{10}). Due to the component $\ln(2x_9^2 + 0.02)$, there are two peaks along variable x_9. By plotting the cross-sectional view of the last two dimensions, we can observe this shape.

We generate a training dataset of 20k points using the SRK method, with a terminal time $T = 1$ and $N = 100$ time steps. The initial distribution $p_0(\boldsymbol{x})$ is a 10-dimensional standard Gaussian distribution and the domain is defined as $[-1.2, 1.2]^{10}$. The test dataset is created using a learning rate of 1×10^{-3} and a threshold of $\epsilon = 1 \times 10^{-8}$ to ensure that densities of all 10k points exceed ϵ. In FPNN, both TNN and MLP architecture successfully learn the two peaks in the x_9 axis, while PINN and TFFN fail to capture this feature. It is evidenced by the divergence between model predictions and true solutions for TFFN in Figure 4. The normalization condition influence the representational capacity and optimization process of models, as discussed in Sec. 1. This results in poor performance of existing methods for 4-6 dimensional SFP equations and failure in higher-dimensional problems.

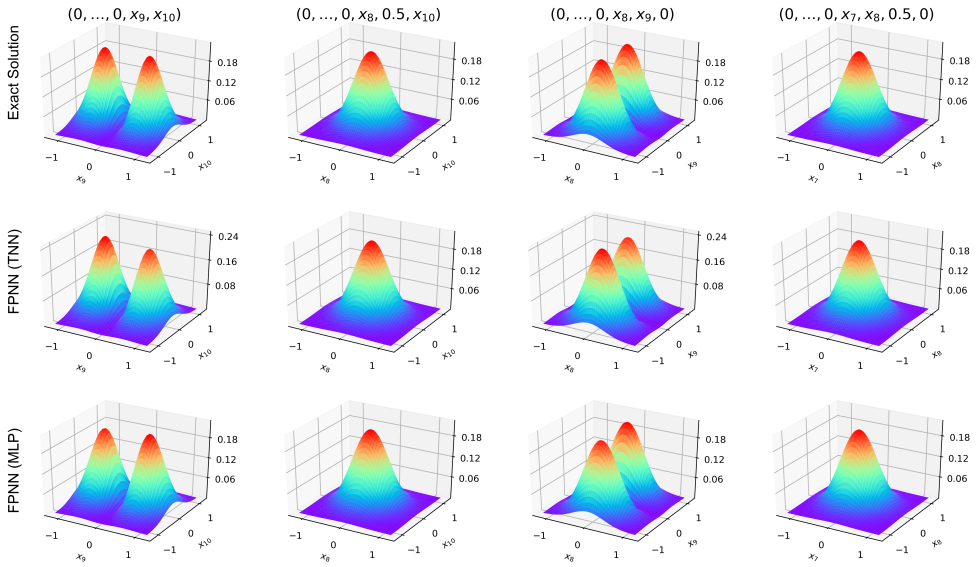

Figure 18: 10D Multi-modal: the exact solution and predicted solutions of FPNN. *Top*: the exact solution. *Middle*: TNN-based FPNN. *Bottom*: MLP-based FPNN.

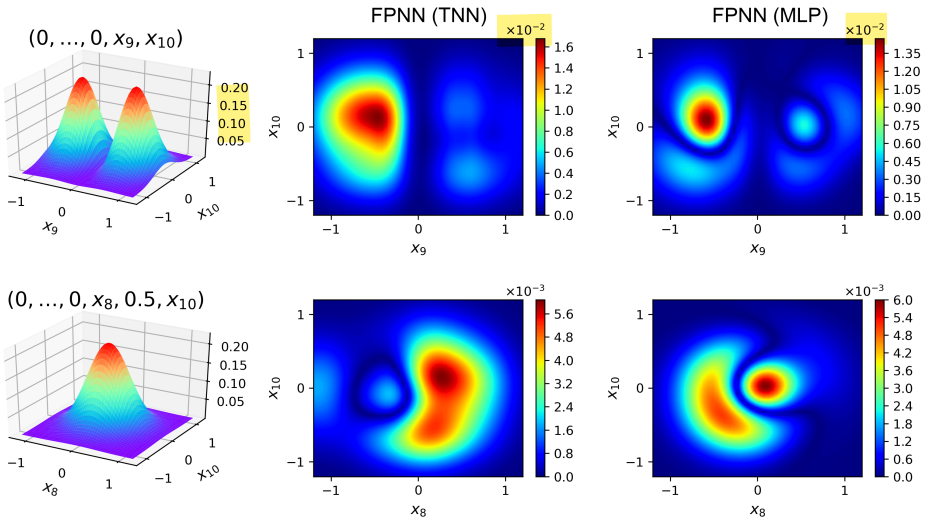

Figure 19: 10D Multi-modal: MAE between the exact solution and predicted solutions of different models. *Left*: the exact solution. *Middle*: TNN-based FPNN. *Right*: MLP-based FPNN.

C.5 10D Gaussian mixture

Following the test problem with two peaks (Tang et al., 2022), we construct a Gaussian mixture distribution $p(\boldsymbol{x}) = \beta_1 p_1(\boldsymbol{x}) + \beta_2 p_2(\boldsymbol{x})$, comprised of two 10-dimensional Gaussian distributions p_1 and p_2. For $k = 1, 2$, each $p_k(\boldsymbol{x})$ is defined by a probability density function with mean μ_k and covariance matrix Σ_k:

$$\beta_1 = 0.55, \quad \mu_1 = [-1.5, -0.8, 1.3, 0.2, -0.1, 0, 0, 0, 0, 0], \quad \Sigma_1 = \begin{pmatrix} \Sigma_{11} & & & \\ & \Sigma_{12} & & \\ & & \Sigma_{13} & \\ & & & \Sigma_{14} \end{pmatrix}$$

$$\Sigma_{11} = \begin{pmatrix} 2.2 & 0 & 0 \\ 0 & 1.2 & 0 \\ 0 & 0 & 2 \end{pmatrix}, \Sigma_{12} = \begin{pmatrix} 1.5 & 0.2 & 0.4 \\ -0.1 & 1.2 & 0.4 \\ -0.2 & -0.2 & 0.8 \end{pmatrix}, \Sigma_{13} = \begin{pmatrix} 0.4 & 0.3 \\ 0.3 & 0.9 \end{pmatrix}, \Sigma_{14} = \begin{pmatrix} 1 & 0 \\ 0 & 1 \end{pmatrix} \tag{39}$$

$$\beta_2 = 0.45, \quad \mu_2 = [1.2, 1, -1.5, 0, 0, 0.1, 0, 0, 0, 0], \quad \Sigma_2 = \begin{pmatrix} \Sigma_{21} & & & \\ & \Sigma_{22} & & \\ & & \Sigma_{23} & \\ & & & \Sigma_{24} \end{pmatrix}$$

$$\Sigma_{21} = \begin{pmatrix} 2.2 & 0 & 0 \\ 0 & 1 & 0 \\ 0 & 0 & 1.5 \end{pmatrix}, \Sigma_{22} = \begin{pmatrix} 1.2 & 0.4 & -0.2 \\ -0.4 & 1.2 & -0.3 \\ 0.2 & -0.1 & 1.2 \end{pmatrix}, \quad \Sigma_{23} = \begin{pmatrix} 0.8 & 0 \\ 0 & 0.3 \end{pmatrix}, \Sigma_{24} = \begin{pmatrix} 1 & 0 \\ 0 & 1 \end{pmatrix} \tag{40}$$

The matrices Σ_1 and Σ_2 are positive definite. FPNN remains applicable for more randomly constructed Gaussian components. To improve visualization, we make some modifications to the mean μ_1, μ_2. First, two Gaussian peaks are placed at a certain distance apart and have different relative positions on the (x_1, x_2) and (x_1, x_3) planes. Secondly, we set the last seven components of the mean near zero, so that we examine the cross-sections $(x_1, x_2, 0, \ldots, 0)$ and $(x_1, 0, x_3, 0, \ldots, 0)$ to reflect the high-density regions of exact solution. It is straightforward to verify that $p(\boldsymbol{x})$ serves as the true solution to following SFP equation:

$$-\nabla \cdot (p(\boldsymbol{x}) \nabla \log(\beta_1 p_1(\boldsymbol{x}) + \beta_2 p_2(\boldsymbol{x}))) + \nabla^2 p(\boldsymbol{x}) = 0 \tag{41}$$

where we get the corresponding drift $\boldsymbol{\mu}(\boldsymbol{x}) = \nabla \log(\beta_1 p_1(\boldsymbol{x}) + \beta_2 p_2(\boldsymbol{x}))$ and diffusion $\boldsymbol{D} = \boldsymbol{I}_{10}$.

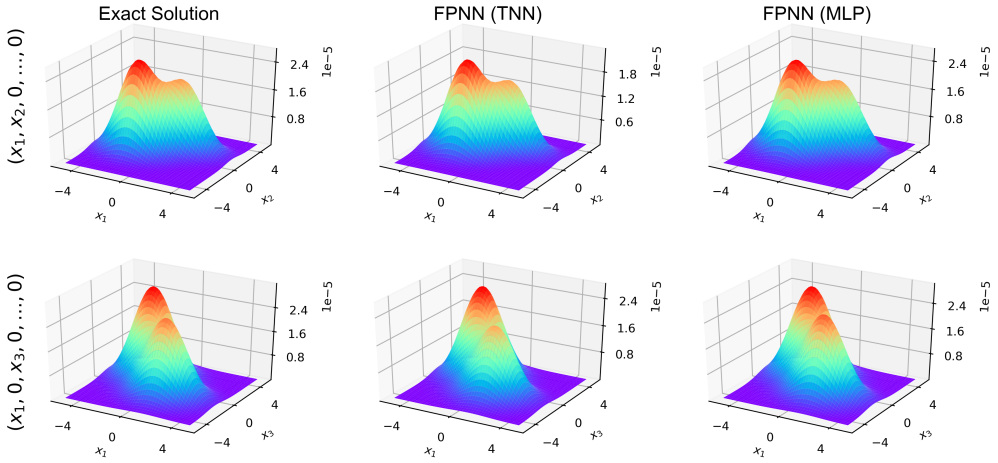

Figure 20: 10D Gaussian mixture: the exact solution and predicted solutions of FPNN. *Left*: the exact solution. *Middle*: TNN-based FPNN. *Right*: MLP-based FPNN.

As the region expands, the stochastic system takes longer to reach a steady state. We select a terminal time of $T = 5$ and $N = 500$ time steps. 20*k* data points are sampled from a 10-dimensional standard Gaussian distribution to serve as the initial set, followed by the SRK method to obtain the target distribution p_T and domain $\Omega = [-5, 5]^{10}$. The test dataset with 10*k* points is sampled from two Gaussian distributions according to weights.

Notably, even though the true solution has the order of 10^{-5}, simple network architectures such as TNN and MLP successfully learn the two Gaussian peaks located on the coordinate planes

$(x_1, x_2, 0, \ldots, 0)$ and $(x_1, 0, x_3, 0, \ldots, 0)$ at 600 and 400 steps, ultimately achieving a mean relative error of 1.86×10^{-7} and 1.16×10^{-7}, respectively. And MLP reaches a MAPE of 18.38% with only 1,480 parameters. The final prediction results and corresponding MAE are presented in Figure 20 and Figure 21.

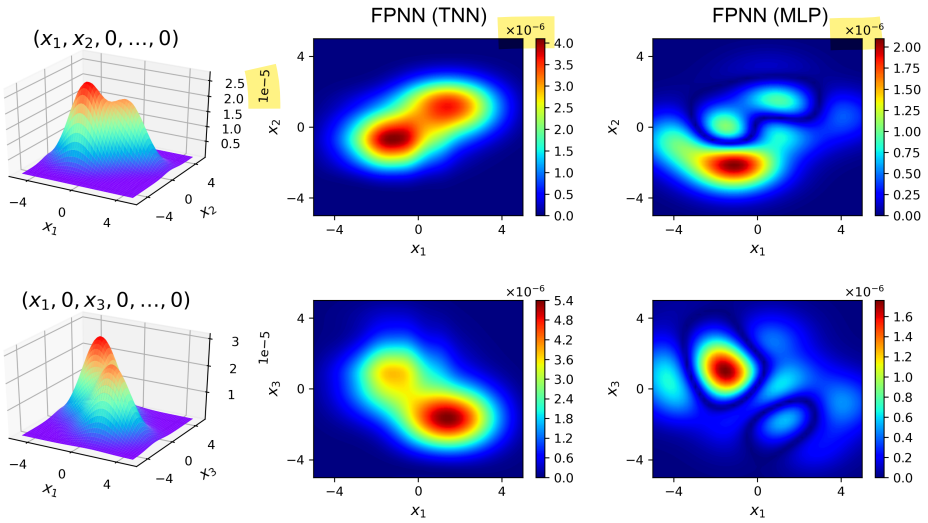

Figure 21: 10D Gaussian mixture: MAE between the exact solution and predicted solutions of different models. *Left*: the exact solution. *Middle*: TNN-based FPNN. *Right*: MLP-based FPNN.

C.6 20D Gaussian

Finally, we consider a SFP equation with drift term $\boldsymbol{\mu}(\boldsymbol{x}) = -a\boldsymbol{x}$ and diffusion matrix $\boldsymbol{D} = \frac{\sigma^2}{2}\boldsymbol{I}_d$. The exact solution is expressed as follows:

$$p(\boldsymbol{x}) = \left(\frac{a}{\pi\sigma^2}\right)^{d/2} \exp\left(-\frac{a\|\boldsymbol{x}\|_2^2}{\sigma^2}\right) \tag{42}$$

In our experiments, we select $d = 20$, $a = 3$ and $\sigma = 1.5$ to test our FPNN with TNN network. So the true PDF is a 20-dimensional Gaussian distribution with zero mean and covariance matrix $\frac{\sigma^2}{2a}\boldsymbol{I}_{20}$. The training dataset is generated by the SRK method, yielding $20k$ samples with $T = 1$ and $N = 100$. Since the initial distribution is chosen as a 20-dimensional standard Gaussian distribution, the drift effect towards the origin dominates, causing particles to converge towards $\Omega = [-2, 2]^{20}$ during the SDE simulation. The test dataset is directly constructed by sampling $10k$ points from the true distribution.

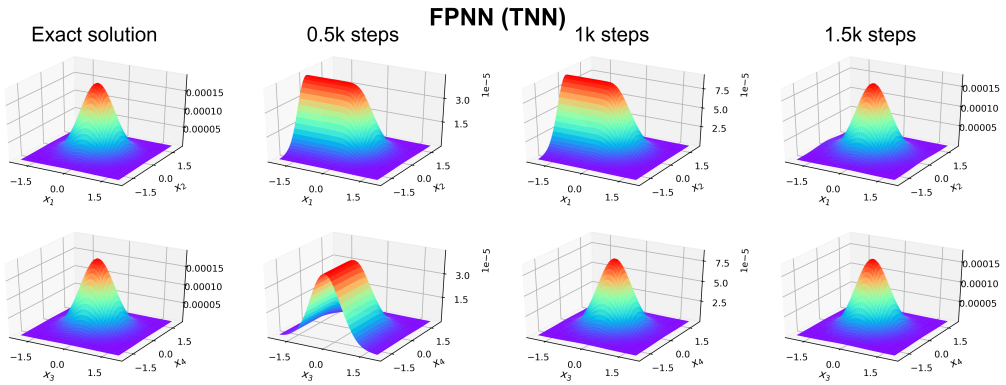

Figure 22: 20D Gaussian: the predicted solution of FPNN during training.

After 1.5k update steps, FPNN successfully learns a 20-dimensional Gaussian distribution, achieving a MAPE of 23.29%. As shown in Figure 10, each dimension aligns well with the true solution, demonstrating both the effectiveness of our method and the validity of evaluation metrics.

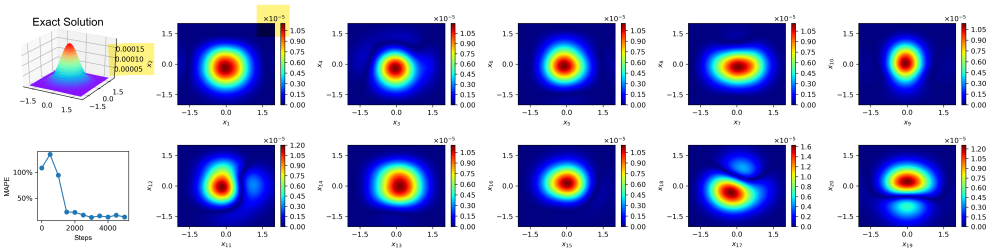

Figure 23: 20D Gaussian: MAE between the exact solution and predicted solution of FPNN. The first column shows the exact solution and the changes of MAPE during training. The remaining parts display MAE for pairs of adjacent dimensions, such as $(x_1, x_2, 0, \ldots, 0)$, $(0, 0, x_3, x_4, 0, \ldots, 0)$, and so on.